

Internally Mediated Developmental Desynchronization of Neocortical Network Activity

Peyman Golshani,¹ J. Tiago Gonçalves,¹ Sattar Khoshkoo,¹ Ricardo Mostany,¹ Stelios Smirnakis,^{3,4} and Carlos Portera-Cailliau^{1,2}

Departments of ¹Neurology and ²Neurobiology, David Geffen School of Medicine at University of California, Los Angeles, Los Angeles, California 90095, and Departments of ³Neurology and ⁴Neuroscience, Baylor College of Medicine, Houston, Texas 77030

During neocortical development, neurons exhibit highly synchronized patterns of spontaneous activity, with correlated bursts of action potential firing dominating network activity. This early activity is eventually replaced by more sparse and decorrelated firing of cortical neurons, which modeling studies predict is a network state that is better suited for efficient neural coding. The precise time course and mechanisms of this crucial transition in cortical network activity have not been characterized *in vivo*. We used *in vivo* two-photon calcium imaging in combination with whole-cell recordings in both unanesthetized and anesthetized mice to monitor how spontaneous activity patterns in ensembles of layer 2/3 neurons of barrel cortex mature during postnatal development. We find that, as early as postnatal day 4, activity is highly synchronous within local clusters of neurons. At the end of the second postnatal week, neocortical networks undergo a transition to a much more desynchronized state that lacks a clear spatial structure. Strikingly, deprivation of sensory input from the periphery had no effect on the time course of this transition. Therefore, developmental desynchronization of spontaneous neuronal activity is a fundamental network transition in the neocortex that appears to be intrinsically generated.

Introduction

Neurons in the developing cerebral cortex exhibit highly synchronized patterns of spontaneous electrical activity (Khazipov and Luhmann, 2006). In neonatal rodents, this early network activity in neocortex is dominated by correlated bursts of action potential firing (Garaschuk et al., 2000; Khazipov et al., 2004). In humans, very similar intermittent bursts of activity separated by long periods of electrical silence (“tracé discontinu”) can be recorded in the electroencephalogram of premature babies (Dreyfus-Brisac and Larroche, 1971). In contrast, activity in the mature neocortex is characterized by more sparse and decorrelated neuronal firing (Stosiek et al., 2003; Kerr et al., 2005; Hromádka et al., 2008), which according to modeling studies is a network state that allows for more efficient neural coding (Shadlen and Newsome, 1994; Zohary et al., 1994; Olshausen and

Field, 2004). The mechanisms underlying this crucial transition from synchronized to decorrelated cortical network activity have not been characterized *in vivo*. One possibility is that sensory-driven activity, which is essential for the proper formation and refinement of neocortical maps (Katz and Shatz, 1996), also drives the desynchronization of cortical network activity. Alternatively, experience-independent (but neuronal activity-dependent factors) could trigger the transition, via mechanisms intrinsic to the neocortex.

The role of early synchronous activity in the developing neocortex is also poorly understood. Just as spontaneous waves of activity in the retina help to drive the formation of eye-specific layers in the lateral geniculate nucleus before eye opening (Shatz and Stryker, 1988), correlated neuronal firing in neocortex could promote the refinement of cortical maps by strengthening of connections between neurons that are coactive through Hebbian mechanisms (Miller, 1994; Miller et al., 1999; Song and Abbott, 2001; Kayser and Miller, 2002). Indeed, silencing this early activity in visual cortex completely blocks the maturation of orientation selectivity (Chapman and Stryker, 1993). To appreciate how spontaneous activity shapes cortical circuits, it is essential to understand how the spatial and temporal correlational structure of ongoing activity changes in the intact developing neocortex. To date, no study has examined the correlational structure of early network activity with single-cell resolution in unanesthetized animals.

Using *in vivo* two-photon calcium imaging and *in vivo* whole-cell recordings in unanesthetized and anesthetized mice, we recorded spontaneous activity patterns in ensembles of layer (L) 2/3 neurons of barrel cortex during postnatal development. We find that these networks undergo a transition from a highly cor-

Received April 28, 2009; revised June 12, 2009; accepted July 24, 2009.

This work was supported by grants from the National Institutes of Health [National Institute of Child Health and Human Development (C.P.-C.) and National Institute of Neurological Disorders and Stroke (P.G.)], the Howard Hughes Medical Institute (S.S.), FRAXA (C.P.-C.), and the Dana Foundation (C.P.-C.). The generous support of the Fu-Hsing and Jyu-Yuan Chen Family Foundation is gratefully acknowledged. We thank Rafael Yuste, Thanos Siapas, Dean Buonomano, Felix Schweizer, Claude Wasterlain, Philipp Berens, Marc Suchard, Alberto Cruz-Martin, and other members of the Portera-Cailliau laboratory for helpful discussions. We thank Shiva Portonovo and Josh Trachtenberg for invaluable help building the microscope, Tara Chowdhury for technical assistance, Karel Svoboda for providing the ScanImage software, and Rainer Friedrich for MATLAB code implementing temporal deconvolution of calcium signals.

P.G., S.S., and C.P.-C. designed the experiments. P.G., J.T.G., S.K., R.M., and C.P.-C. performed the experiments. P.G., J.T.G., S.S., and C.P.-C. analyzed the data. P.G., R.M., S.K., S.S., and C.P.-C. generated the figures. P.G., S.S., and C.P.-C. wrote the manuscript.

Correspondence should be addressed to either Peyman Golshani or Carlos Portera-Cailliau, Department of Neurology, David Geffen School of Medicine at University of California, Los Angeles, Los Angeles, 710 Westwood Plaza, Los Angeles, California 90095. E-mail: pggolshani@mednet.ucla.edu or cpcailiau@mednet.ucla.edu.

DOI:10.1523/JNEUROSCI.2012-09.2009

Copyright © 2009 Society for Neuroscience 0270-6474/09/2910890-10\$15.00/0

related to a much more decorrelated state at the end of the second postnatal week. Removing sensory inputs did not alter the magnitude, timing, or spatial structure of the desynchronization, suggesting that it is mediated internally by the neocortex.

Materials and Methods

All materials were purchased from Sigma-Aldrich unless otherwise stated. All experiments were performed under animal protocols approved by the Animal Research Committee and the Office for the Protection of Research Subjects at the University of California, Los Angeles.

Cranial window surgery. We used male and female C57BL/6 mice at ages postnatal day 4 (P4) to adult (we considered mice to be adults after P30). Mice were anesthetized with isoflurane (1.5% via a nose cone) or urethane (1.5 g/kg, i.p.) and placed in a stereotaxic frame. An ~2-mm-diameter craniotomy was performed over the primary somatosensory barrel cortex and partially covered with a glass coverslip, as described previously (Garaschuk et al., 2006; Sato et al., 2007), except that no agarose was used. Care was taken not to damage the dura or underlying vessels during the procedure. A well was made from dental cement around the cranial window to hold a meniscus of cortex buffer, pH 7.4 (in mM: 125 NaCl, 5 KCl, 10 glucose, 10 HEPES, 2 CaCl₂, and 2 MgSO₄) for the water-dipping objective. For experiments including electrophysiological recordings, a silver-chloride ground wire insulated with Teflon (except at the tip) was passed through a burr hole over the cerebellum and fixed with dental cement. A titanium bar (0.125 × 0.375 × 0.05 inch) was also attached to the skull with dental cement to secure the animal to the microscope stage. All skin incision points were infiltrated with lidocaine, and skin edges were sealed with dental cement.

Preparation of animals for unanesthetized recordings. P4–P14 mice were allowed to awaken from anesthesia in the recording chamber on a heating pad at 37°C. These young mice typically remained calm while head fixed, allowing calcium imaging experiments that lasted 1–2 h. Animals older than P14 were extensively handled for 10–20 min until they ran freely from hand to hand. They were then placed on an 8 inch spherical treadmill (loosely adapted from Dombek et al., 2007) and were allowed to move freely as the investigator moved the spherical treadmill to keep the mice on the apex of the ball. After mice acclimated to the treadmill, we implanted cranial windows under isoflurane anesthesia and transferred the mice to the microscope in which they were head fixed and allowed to awaken. After ~10–20 min, mice became acclimated to running or resting on the spherical treadmill. Calcium imaging could be performed for 1–2 h during periods when mice sat quietly. During brief moments of grooming or walking on the treadmill (typically lasting no more than 5–10 s over a 3 min movie), motion artifacts in the collected images prevented interpretation of the calcium transients (see below). Mice did not exhibit signs of pain or distress during the *in vivo* imaging or electrophysiological recordings.

In vivo two-photon calcium imaging. Please refer to JoVE video article by Golshani and Portera-Cailliau (2008) for details of the procedure. P4–P14 mice were transferred to the microscope stage and head fixed. Mice older than P14 were acclimated to a spherical treadmill before placement of the cranial window (see above). A total of 1 mM Oregon-Green BAPTA-1 AM (OGB) or Fluo-4 AM (Invitrogen) were mixed in DMSO/Pluronic as described previously (Stosiek et al., 2003) and mixed with 40 μM Alexa-594 (Invitrogen) to allow visualization of the pipette during injection or 100 μM sulforhodamine-101 (SR) (Invitrogen) to visualize astrocytes. SR was included in all experiments involving unanesthetized animals and in 15 of 42 experiments involving anesthetized animals. When SR was not used, astrocytes could readily be recognized by their unique morphology and very slow calcium transients. Glass microelectrode pipettes (2–4 MΩ) were pulled (P-97; Sutter Instruments) and filled with the OGB solution. The calcium indicator solution was pressure injected at 10 psi for 1 min (Picospritzer; General Valve), at a depth of 200 μm below the dura. Typically two to four injections, spaced 200–300 μm apart, were needed to label an area measuring 600 × 600 μm in the *x-y* plane. Calcium imaging was begun ~1 h after injection with a custom-built two-photon microscope using a titanium-sapphire laser (Chameleon XR; Coherent) tuned to 800–880 nm.

Images were acquired using ScanImage software (Pologruto et al., 2003) written in MATLAB (MathWorks). Laser power was typically maintained well below 70 mW at the sample. Whole-field images were collected either using a 20×, 0.95 numerical aperture or 40×, 0.8 numerical aperture objectives (Olympus) at various acquisition speeds, ranging from 3.9 Hz (128–512 × 128 pixels) to 15.6 Hz (128–512 × 32 pixels). We generally imaged 100–200 neurons simultaneously during each imaging session, depending on the speed of image acquisition and age of the mouse (more neurons could be imaged at younger ages because they were more tightly packed). Overall, the data presented from unanesthetized mice (see Figs. 1, 2) were obtained from a total of 707 neurons in four mice at P4–P7, 527 neurons in five mice at P8–P11, 712 neurons in six mice at P12–P15, and 243 neurons in four mice older than P16. Typically, 5–10 3-min movies were acquired. A subset of experiments examining the relationship of domains of coactivated cells to underlying barrels at P5–P7 (see Figs. 2E, 3) were performed at ~2.0 fps (512 × 256 pixels) to image a larger field of view (~650 × 325 μm). For experiments in anesthetized animals, we used urethane (1.5 g/kg) or light isoflurane anesthesia (0.5–0.8%) during the calcium imaging, and mice were kept at 37°C using a temperature-control device with a rectal probe (Harvard Apparatus). With isoflurane, the respiratory rate of the animals was kept at 90–100 breaths/min. With urethane, mice were given additional intraperitoneal injections at 20% of the original dose when foot-withdrawal reflexes returned, typically after ~2–3 h. For experiments with unanesthetized animals, imaging was begun 30 min to 1 h after the discontinuation of isoflurane.

Data analysis. Calcium imaging data were analyzed using routines custom-written in NIH ImageJ and MATLAB. Neuronal somatic traces were deconvolved using a well established temporal deconvolution algorithm (Yaksi and Friedrich, 2006). Several 3 min movies were concatenated, and brief segments of motion artifact in recordings from unanesthetized mice were removed as needed (totaling <10% of the total movie length). To correct for slight *x-y* drift, movies were then aligned using the Stackreg plugin for NIH ImageJ (bigwww.epfl.ch/thevenaz/stackreg). An average intensity *t*-stack projection image of the entire movie was created, within which contours around OGB-labeled cells were automatically detected and drawn using custom algorithms (occasionally, contours of cells lying close together were separated by a line drawn manually). Neuronal and neuropil signals were analyzed separately. Astrocytic signals were excluded from analysis. The average $\Delta F/F$ signal of each cell body was calculated at each time point. Each $\Delta F/F$ trace was low-pass filtered using a Butterworth filter (coefficient of 0.16) and deconvolved with a 2 s single-exponential kernel for experiments using OGB and a 1 s single exponential for experiments using Fluo-4, as described previously (Yaksi and Friedrich, 2006). The SD of all points below zero in each deconvolved trace was calculated, multiplied by two, and set as the positive threshold level below which all points in the deconvolved trace were set to zero. These parameters were set after control experiments using simultaneous loose cell-attached recordings and calcium imaging demonstrated optimal correlation between spike trains and deconvolved traces at these settings. For experiments assessing the reliability of temporal deconvolution in detecting changes in the firing rate of neurons, firing rates obtained by electrophysiological recordings were smoothed with a 400 ms sliding window when the imaging frequency was 15.6 Hz and a 1000 ms sliding window when the imaging frequency was 3.9 Hz. For experiments involving OGB, the estimated firing rate of neurons was obtained by multiplying the deconvolved trace by the factor 78.4, which was derived empirically from cell-attached recordings (scaling factor, 78.4 ± 10.3; *n* = 5 cells). For experiments involving Fluo-4, the estimated firing rate was obtained by multiplying the deconvolved trace by the factor 148.6, which was also derived empirically from cell-attached recordings (scaling factor, 148.6 ± 40.7; *n* = 3 cells). Pairwise cross-correlations between each pair of deconvolved traces were performed, and a correlation coefficient normalized to the autocorrelation at zero lag was recorded. This correlation coefficient was calculated using the formula $(A \times B)/[\text{norm}(A) * \text{norm}(B)]$, where *A* and *B* represent deconvolved somatic calcium vectors from a pair of cells whose correlation coefficient is being calculated and “norm” outputs the Euclidean length of each

vector. Analysis was also performed using Pearson's correlation coefficients, and the results were identical.

To determine whether correlation coefficients between cell pairs were statistically significant, we temporally displaced each deconvolved somatic calcium trace 100 times randomly with respect to the other traces using a SHIFT algorithm as described previously (Louie and Wilson, 2001). Next, we calculated the correlation coefficient between all pairs of shifted deconvolved traces. Cell pairs with a correlation coefficient greater than the 95th percentile of correlation coefficients in the randomized sample were deemed statistically significant ($p < 0.05$).

To obtain a more unbiased characterization of the network dynamics, we performed singular value decomposition (Golomb et al., 1994) in MATLAB on each deconvolved firing rate matrix (supplemental Fig. S3, available at www.jneurosci.org as supplemental material). The mean firing rate of each cell was first subtracted from each firing rate vector. Singular values were obtained from each matrix and from 100 surrogate matrices obtained by circularly shuffling each firing rate vector as above. We calculated the ratio of each singular value squared (the eigenvalue) obtained from the actual experimental data to the median eigenvalue obtained from the shuffled traces. These values, especially those obtained for the first 5–10 singular values, reflected the magnitude of the correlations in each matrix.

To calculate frequency, duration, and estimated firing rates during network events, we first marked the temporal boundaries of network events. This was performed by first constructing activity histograms that plotted the percentage of cells that were active for each frame of each movie (frames acquired every 64–256 ms). The threshold for detection of a network event was set by repeatedly shuffling each deconvolved somatic calcium trace 100 times while maintaining the average firing rate for each cell constant. A surrogate activity histogram was constructed from each reshuffled trial. The threshold was calculated by first finding the peak percentage of cells active in each reshuffled trial and then sorting these values to find the 95th percentile, which was set as the threshold for significance ($p = 0.05$). The time point when the percentage of cells active exceeded this threshold was set as the start of an event, and the time point when the percentage of cells active fell below this level was set as the end of the event.

For calcium imaging experiments, all cells within an animal were averaged, and the mean of means was calculated for each developmental stage and treatment group. Therefore, in all figures, n represents the number of animals. All data are expressed as mean \pm SEM.

Electrophysiology. *In vivo* patch-clamp recordings in whole-cell or cell-attached configurations were performed using a patch-clamp amplifier (Multiclamp; Molecular Devices). We performed cell-attached recordings simultaneously with calcium imaging under several imaging conditions that were identical to the imaging conditions we used throughout the study (supplemental Table 1, available at www.jneurosci.org as supplemental material). In general, imaging with OGB had lower single spike detection (defined as a spike occurring < 300 ms from another spike) than Fluo-4, but it accurately reported ($> 80\%$) spike doublets and bursts of three or more spikes at all acquisition frequencies. Imaging with Fluo-4 resulted in reliable ($> 85\%$) single action potential detection. The deconvolved traces obtained with either indicator showed good correlation to actual spike density functions obtained by electrophysiology (supplemental Table 1, available at www.jneurosci.org as supplemental material), with Fluo-4 showing the best correlation ($r > 0.85$). Nevertheless, we performed the bulk of experiments with OGB, because Fluo-4 failed to stain large populations of neurons, and its signal faded quickly. Furthermore, using a simple computer simulation (see below, Simulations), we determined that excluding the proportion of single action potentials missed by our detection algorithm had a negligible effect on the correlation coefficients that we measured at both the early and late developmental stages (supplemental Fig. S1G, available at www.jneurosci.org as supplemental material). This suggests that correlation coefficients are mainly determined by bursts of two or more action potentials.

Current-clamp recordings were performed with borosilicate microelectrodes (4–6 M Ω) using a potassium gluconate-based solution (in mM): 105 K-gluconate, 30 KCl, 10 HEPES, 10 phosphocreatine, 4 ATP-Mg, and 0.3 GTP, adjusted to pH 7.3 with KOH. Voltage-clamp record-

ings were performed with a cesium methanesulfonate-based internal solution (in mM): 135 Cs-methanesulfonate, 8 NaCl, 10 HEPES, 10 Na₂-phosphocreatine, 0.3 Na-GTP, and 10 QX-314 [2-(triethylamino)-N-(2,6-dimethylphenyl) acetamine] (to block voltage-gated sodium channels), and 0.02 Alexa 594. Action currents were not observed during voltage-clamp recordings. A subset of neurons ($n = 6$) recorded in whole-cell mode were successfully filled with Alexa-594 and identified as L2/3 pyramidal neurons by two-photon microscopy. For whole-cell recordings, series resistance was typically between 30 and 80 M Ω . The holding potential in voltage-clamp recordings was corrected for series resistance error. A 5 mV junction potential was subtracted from the corrected holding potentials in voltage-clamp recordings. Data were acquired at 10 kHz, low-pass filtered at 2–6 kHz, and analyzed using custom-written routines in MATLAB. Loose cell-attached recordings were also performed to record the spiking of neurons. Input resistance of the neurons was estimated by measuring the maximum voltage change in response to a hyperpolarizing 25 pA pulse during periods when the membrane potential of the neuron was hyperpolarized (i.e., a “down” state). To determine the balance of excitation and inhibition during recurrent network events, we determined the extrapolated reversal potential of the peak amplitude as well as the charge transfer under voltage-clamp conditions. Because the reversal potential for excitatory transmission is near 0 mV whereas that of inhibitory transmission is at the calculated chloride reversal potential (approximately -70 mV), the relative distance of the reversal potential (i.e., “up” state) of the network event from these two membrane potentials informed us of the relative balance of excitation and inhibition.

Simulations. A simplified 100 neuron system was simulated in MATLAB. The frequency of network events was set from our raw electrophysiological data at different postnatal ages. Each network event in a given neuron was assigned a certain probability of resulting in the firing of zero to five spikes. These probabilities were also assigned based on the electrophysiology data. The spikes were set to occur at random times within each network event. Spikes were binned into 50 ms intervals and smoothed with 400 ms sliding window to simulate the temporal precision of deconvolved calcium signals. Correlation coefficients were then calculated at zero lag between every pair of smoothed firing rate vectors to obtain a simulated cross-correlation matrix.

Sensory deprivation. Starting from P2 to P3, animals were anesthetized with isoflurane, and all the principal whiskers contralateral to imaged hemisphere were removed under a dissecting microscope by grasping each whisker with forceps and applying gentle pulling pressure until the whisker was removed. This procedure was repeated every other day until the animals were imaged.

Anatomical reconstructions. Mice were anesthetized with a lethal dose of ketamine (120 mg/kg) and xylazine (15 mg/kg) and perfused transcardially with 4% paraformaldehyde (PF) in 0.1 M phosphate buffer, pH 7.4. The brain was postfixed overnight in 4% PF, and 50 μ m slices were cut tangentially in the same plane as imaging. The imaged region was reconstructed as described previously (Holtmaat et al., 2006). Extreme care was taken to preserve the most superficial slices in which the imprint of the pial and dural vessels was visible. Slices were then processed for cytochrome oxidase histochemistry to label barrel-related patterns in L4 (Iwasato et al., 1997) and then Nissl stained with cresyl violet. The pattern of blood vessels seen on the sections was matched to a digital photograph of the same vessels taken through the cranial window when the mouse was being imaged. These vessels were also matched to the silhouettes of the vessels seen on two-photon imaging stacks to precisely identify the locations of all the cells with respect to barrels and septae (supplemental Fig. S7, available at www.jneurosci.org as supplemental material). Cells located at the extreme edge of the barrel were not included in the analysis to reduce potential error introduced by small inaccuracies in our ability to register the images.

Results

Developmental decorrelation of cortical network activity

Using *in vivo* two-photon calcium imaging, we recorded the activity of large ensembles of L2/3 neurons in barrel cortex of unanesthetized and anesthetized mice from P4 to adulthood. We

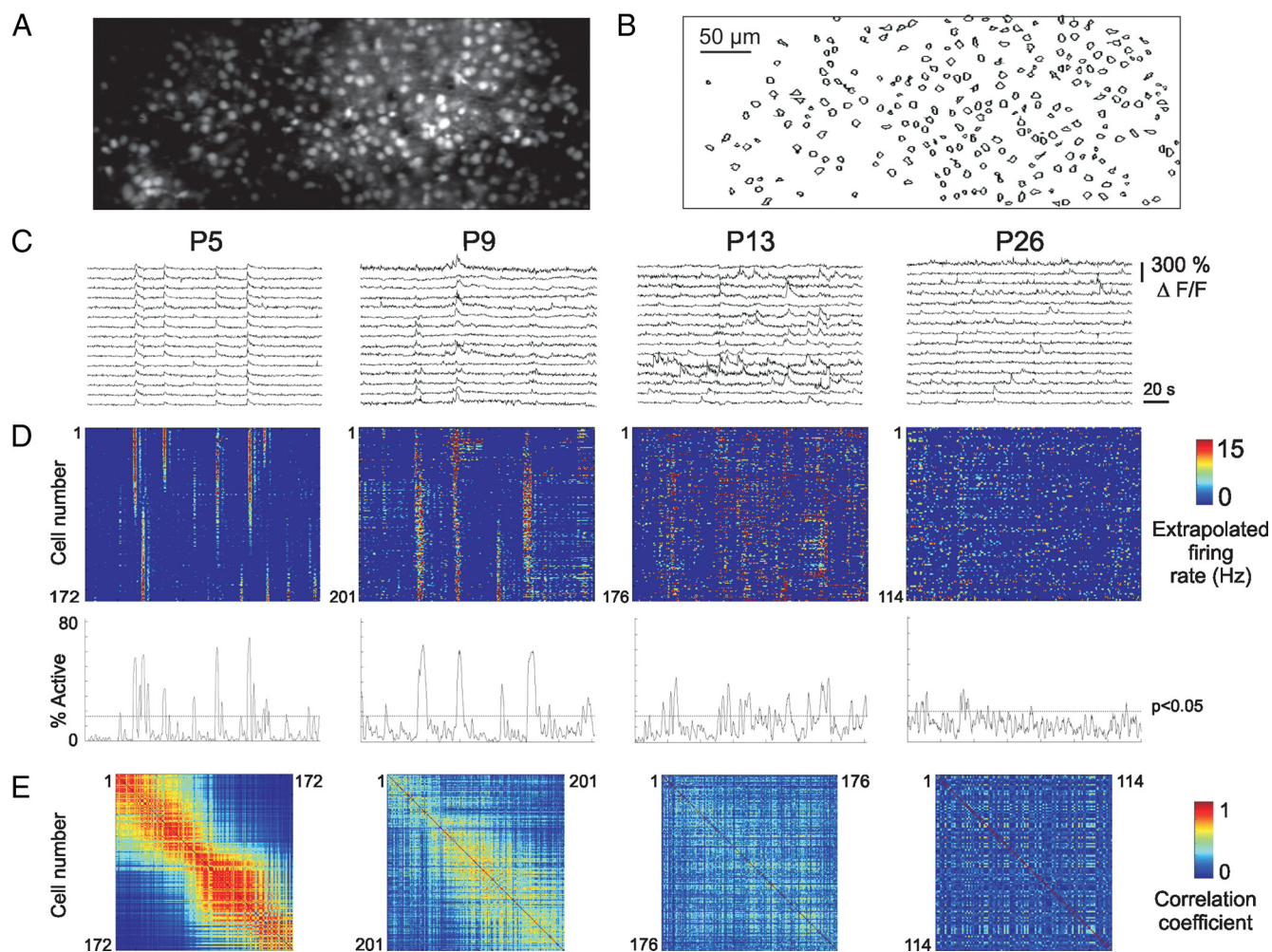


Figure 1. Rapid decorrelation of neuronal activity after P12. **A**, Average intensity projection of a time-lapse “movie” stack of two-photon images of OGB-loaded cells in L2/3 of barrel cortex from a representative *in vivo* experiment (P9 mouse). **B**, Contours of cells automatically detected in the image using custom-written routines in NIH ImageJ and MATLAB. Not all OGB-labeled cells in **A** have a corresponding profile in **B**, because some of the cells were astrocytes. **C**, $\Delta F/F$ calcium traces of 15 individual L2/3 neurons from representative experiments at P5, P9, P13, and P26. Five representative traces for each age group are shown in expanded form in supplemental Figure S2 (available at www.jneurosci.org as supplemental material). **D**, Top, Extrapolated firing rates from deconvolved calcium traces of all neurons in the above experiments. Bottom, Percentage of neurons active across time. Dashed line shows the threshold at a significance level of $p = 0.05$ for detection of synchronous network events. **E**, Correlation matrices displaying the correlation coefficients between the deconvolved calcium traces of all possible cell pairs. Cells were ordered sequentially from top to bottom and then from right to left.

performed simultaneous cell-attached electrophysiological recordings and calcium imaging with the fluorescent calcium indicators OGB and Fluo-4 to establish whether we could accurately measure changes in firing rates with single-cell precision (supplemental Fig. S1, available at www.jneurosci.org as supplemental material). We used an established temporal deconvolution algorithm (Yaksi and Friedrich, 2006) to estimate neuronal firing rates from changes in the fluorescence signal and found a high correlation between deconvolved somatic calcium traces and electrophysiological recordings at all ages (P12–P27) (supplemental Table 1, available at www.jneurosci.org as supplemental material). Although Fluo-4 was better than OGB at detecting single spikes, we used OGB for the majority of experiments because more neurons could be stained with OGB and the goal of these studies was to characterize the spatial dynamics of the activity of large ensembles of L2/3 neurons.

At the earliest ages (P4–P7), *in vivo* imaging in unanesthetized mice revealed transient elevations of intracellular calcium in clusters of L2/3 neurons (Fig. 1C,D, P5 example) (supplemental Fig. S2 and Movie 1, available at www.jneurosci.org as supplemental material). Similar events were observed at P8–P11, although

these events seemed to recruit larger neuronal ensembles (supplemental Movie 2, available at www.jneurosci.org as supplemental material). In contrast, by P12–P15 and especially after P16, firing of L2/3 neurons was much less synchronous (Fig. 1C,D, P13 and P26 examples) (supplemental Movies 3, 4, available at www.jneurosci.org as supplemental material). To quantify the magnitude of this change in network behavior, we computed pairwise correlation coefficients for all possible pairs of neurons from the deconvolved calcium traces (Fig. 1E). The mean correlation coefficient of all cell pairs decreased significantly from 0.37 ± 0.05 at P4–P7 to 0.20 ± 0.02 at P12–P15 stages (supplemental Table 2, available at www.jneurosci.org as supplemental material) (one-way ANOVA, $p = 0.0044$; Tukey’s *post hoc* test, $p < 0.05$), suggesting that the critical transition occurs in the second postnatal week. We also used singular value decomposition as an additional unbiased measure of the magnitude of correlated activity (Golomb et al., 1994) and found very similar results (supplemental Fig. S3, available at www.jneurosci.org as supplemental material). Neither the average neuronal firing rate nor the average firing rate during synchronous network events changed significantly during the period we examined;

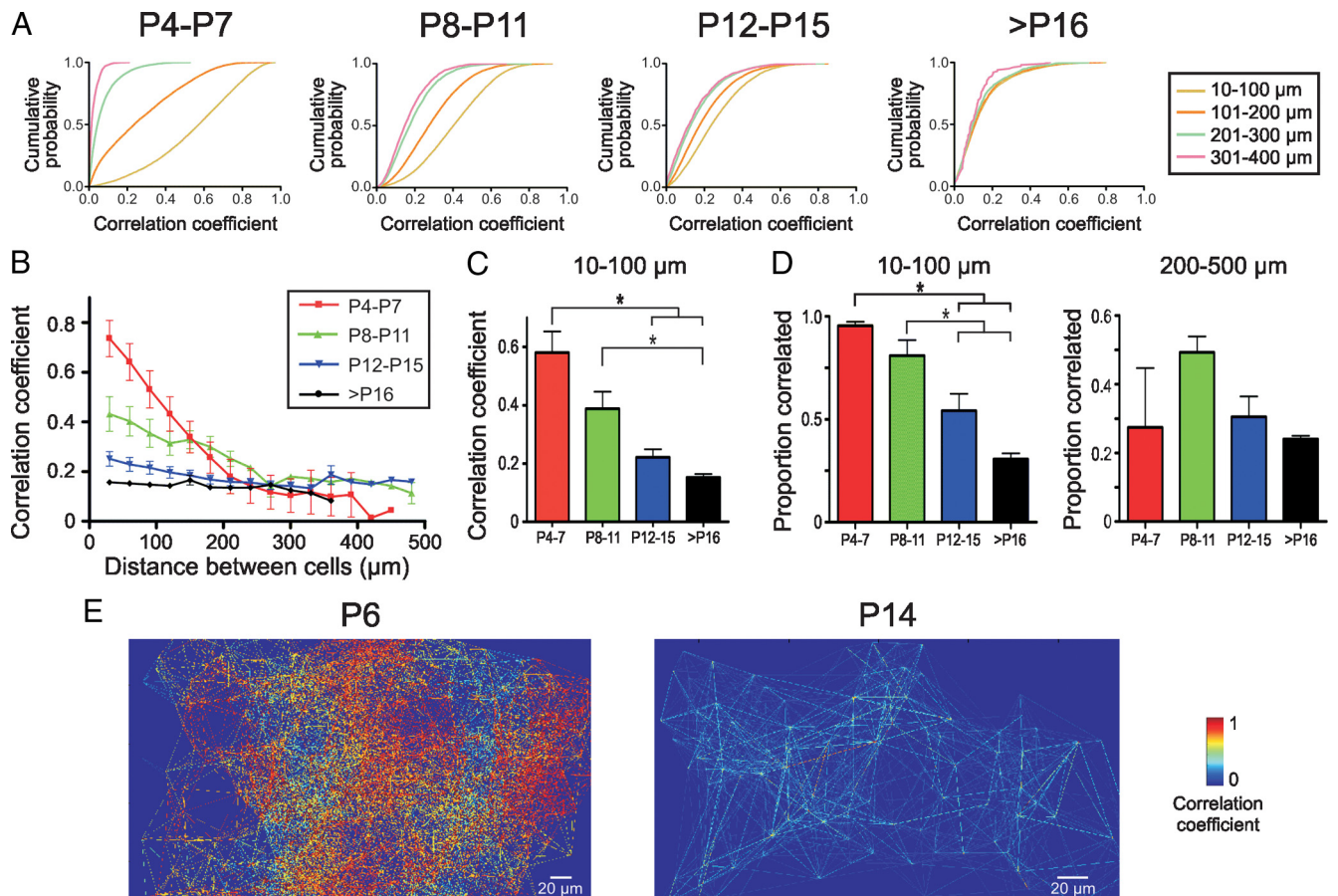


Figure 2. The spatial structure of network activity is developmentally regulated. **A**, Cumulative probability plots of correlation coefficients, pooled according to distance between cell pairs. All data obtained from experiments with OGB in unanesthetized mice at P4–P7 ($n = 4$ mice), P8–P11 ($n = 5$ mice), P12–P15 ($n = 6$ mice), and older than P16 ($n = 4$ mice). **B**, Mean correlation coefficient versus distance separating neuronal pairs. All mice were unanesthetized. **C**, Mean correlation coefficient of cells located within 100 μm from each other at different postnatal ages. **D**, Proportion of significantly correlated neuronal pairs located 10–100 μm from each other (left) or 200–500 μm from each other (right) at different postnatal ages. **E**, Representative spatial correlograms showing the correlation coefficient of cells located within 50 μm of each other for a P6 (left) and a P14 (right) mouse. Lines connecting neuronal pairs are pseudo colored to reflect the amplitude of their correlation coefficient. For **B–D**, correlation coefficients from all cell pairs within an animal were averaged, and the mean of means was calculated for each developmental stage and treatment group. Error bars in **B–D** reflect the SEM. Asterisks in **C** and **D** demonstrate statistical significance using a one-way ANOVA, followed by a Tukey's *post hoc* test.

both stayed at 0.4–0.6 Hz (see Fig. 4D) and 2.5–3.0 Hz (data not shown), respectively.

The average calcium signal from the neuropil correlated strongly with the early network events detected within neuronal cell bodies during the first postnatal week and diminished in amplitude but increased in frequency through the second postnatal week (supplemental Fig. S4A, available at www.jneurosci.org as supplemental material). To ensure that this neuropil signal did not contaminate the somatic calcium signals because of potential signal averaging in the z -plane, we reanalyzed the data ($n = 3$ mice at P8–P11, $n = 3$ mice at P14–P16) by only including cells that were optically sectioned near their equator, in which such contamination is expected to be the lowest (Sato et al., 2007). We still found a robust developmental decorrelation of network activity in these optimally sectioned neurons (supplemental Fig. S4C, available at www.jneurosci.org as supplemental material), indicating that calcium signals from the neuropil did not affect our results.

Spatial structure of ensemble activity in developing cortex

We next examined the spatial structure of ensemble activity in neocortex. At P4–P7, the mean correlation coefficient of cell pairs located within 100 μm of each other was very high ($r =$

0.58 ± 0.07) (Fig. 2A–C), and virtually all ($95.4 \pm 2.0\%$) of these cell pairs were significantly correlated (Fig. 2D). In contrast, the mean correlation coefficient of cell pairs located within 200–500 μm was very low ($r = 0.12 \pm 0.07$) (Fig. 2B), and few of them were significantly correlated ($27.4 \pm 17.2\%$) (Fig. 2D).

In contrast, after P12, the mean correlation coefficient for cell pairs located within 100 μm of each other was significantly lower than at P4–P7 (0.22 ± 0.03 ; one-way ANOVA, $p < 0.0001$; Tukey's *post hoc* test, $p < 0.001$) (Fig. 2A,B). Furthermore, the magnitude of correlations after P12 did not vary with distance separating cell pairs ($p > 0.05$) (Fig. 2B) (supplemental Table 2, available at www.jneurosci.org as supplemental material). Similar results were found when data were normalized for the increase in interneuronal distance that occurs during postnatal development (supplemental Fig. S5, available at www.jneurosci.org as supplemental material). Also, a significant decorrelation of neuronal activity was observed in experiments using Fluo-4 (supplemental Fig. S6, available at www.jneurosci.org as supplemental material), suggesting that this large change in network dynamics was not an artifact of suboptimal spike detection with OGB.

At early postnatal ages, most network events involved small domains of neurons that were surrounded by neurons whose firing was less correlated (Fig. 2E) (supplemental Movie 5, avail-

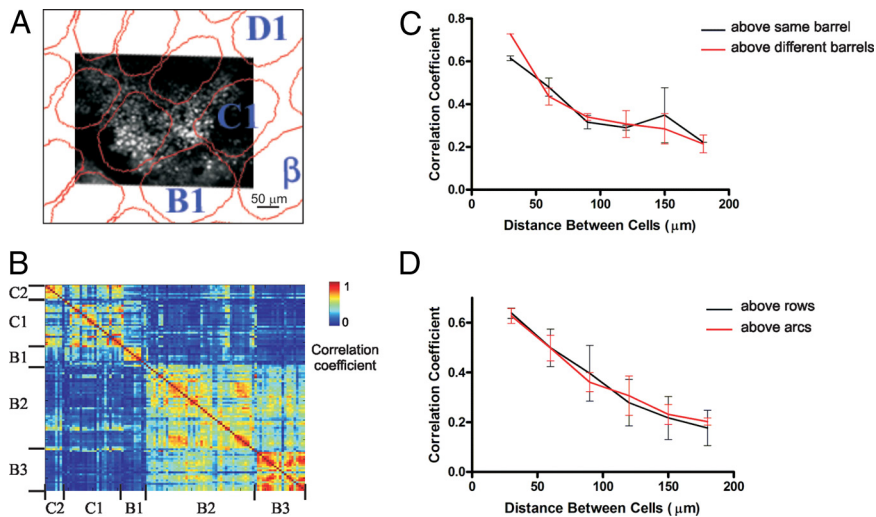


Figure 3. Relationship of network activity to barrel boundaries in L4. **A**, *Post hoc* reconstruction of the L4 barrel cytoarchitecture (from cytochrome oxidase staining) in relationship to the OGB-filled neurons in L2/3 previously imaged with *in vivo* two-photon microscopy in a P6 mouse. **B**, Correlation matrix displaying the correlation coefficients between the estimated firing rate vectors for all possible cell pairs. L2/3 neurons are grouped according to whether they are situated above one barrel or another. Cells residing above septae are not displayed. **C**, Mean correlation coefficient versus distance separating pairs of cells located above the same barrel (black) or above different barrels (red) at P6–P8 ($n = 3$ mice). Error bars in **C** and **D** reflect the SEM. **D**, Mean correlation coefficient versus distance separating pairs of cells located above the same row of barrels (black) or above the same arc of barrels (red) at P6–P8 ($n = 3$ mice).

able at www.jneurosci.org as supplemental material). Given the shape and size (~ 100 – $200 \mu\text{m}$ in diameter) of these neuronal domains, we wondered whether they corresponded to above-barrel clusters of neurons. We performed *post hoc* reconstructions of imaged brains using cytochrome oxidase histochemistry and determined the exact location of each neuron imaged with respect to the underlying barrel columns (supplemental Fig. 7, available at www.jneurosci.org as supplemental material) (Fig. 3A). We then compared the correlation coefficients for groups of cells located above the same barrel versus groups of cells located above different barrels. Although neurons above a given barrel tended to be highly correlated (Fig. 3B), we found that the main determinant of whether two cells fired together was the distance between them because, after normalizing for distance, the correlation coefficients were similar whether cells were located above the same barrel or different barrels (Fig. 3C). Furthermore, correlation coefficients versus distance relationships were similar regardless of whether cells were grouped according to whether they were located above barrel rows or arcs (Fig. 3D). This suggests that the spatial structure of the observed domains of coactive neurons during the first postnatal week does not appear to respect specific barrel boundaries of L4.

Developmental decorrelation persists through changes in neocortical state induced by anesthesia

Recent studies suggest that the degree of neuronal correlations in the mature neocortex is state dependent (Poulet and Petersen, 2008), and anesthesia can have significant effects on network activity (Greenberg et al., 2008). Therefore, we also performed calcium imaging in mice lightly anesthetized with isoflurane (0.5–0.8%) or urethane (1.5 g/kg). Although both anesthetics decreased overall firing rates and shortened the duration of network events (Fig. 4A, D), interneuronal correlations were only modestly affected (Fig. 4B, C), and the developmental decorrelation of neocortical activity was still readily apparent (Fig. 4E, F). The mean correlation coefficient of cell pairs located $<100 \mu\text{m}$

from each other still decreased dramatically between the P9–P11 and P12–P15 age groups under isoflurane (0.48 ± 0.04 , $n = 5$ vs 0.24 ± 0.05 , $n = 3$, respectively; $p < 0.0001$) and urethane (0.41 ± 0.06 , $n = 5$ vs 0.21 ± 0.01 , $n = 3$, respectively; $p = 0.0028$) (Fig. 4F). Therefore, the desynchronization of spontaneous activity persists through changes in neocortical state induced by anesthesia.

In vivo patch-clamp recordings reveal developmental changes in subthreshold membrane potential dynamics

To investigate the mechanisms underlying this robust and rapid decorrelation of network activity, we performed *in vivo* whole-cell recordings of L2/3 neurons at P6–P20 (supplemental Table 3, available at www.jneurosci.org as supplemental material), in isoflurane anesthetized mice (Fig. 5A) ($n = 16$) and in unanesthetized mice (Fig. 5B) ($n = 5$). None of these neurons were fast-spiking interneurons, and, of the cells we reconstructed ($n = 6$), all were L2/3 pyramidal neurons (data not shown). Neurons at P6–P11 under isoflurane ($n = 5$) showed infrequent (0.04 ± 0.01 Hz) spontaneous depolarizations lasting 1.1 ± 0.4 s. The majority of depolarizations ($68.5 \pm 4.1\%$) resulted in the firing of action potentials. In contrast, after P13 ($n = 11$), there was a striking change in both the subthreshold and suprathreshold membrane potential fluctuations of L2/3 neurons (Fig. 5C). Although the frequency of depolarizations increased more than 10-fold (0.04 ± 0.01 Hz at P6–P11 vs 0.43 ± 0.10 Hz at P13–P18; Student's *t* test, $p < 0.05$), the proportion of depolarizations resulting in action potential firing decreased more than threefold (from $68.5 \pm 4.1\%$ at P6–P10 to $22.6 \pm 3.9\%$ at P13–P18; $p < 0.0001$) (Fig. 5C). This occurred despite a hyperpolarization of the action potential threshold after P13 (-29.1 ± 1.5 mV at P6–P10 vs -37.1 ± 1.9 mV at P13–P18; $p < 0.05$) (Fig. 5C). Computer simulations (see supplemental Methods, available at www.jneurosci.org as supplemental material) showed that such changes in the frequency of network events and in the firing probability per event can account for an approximately fourfold decrease in the mean correlation coefficient of all cell pairs, which is commensurate with what we observed with calcium imaging over the same developmental period.

In vivo whole-cell recordings from unanesthetized mice showed a similar reduction in the probability of action potential firing per depolarization event after P12 (Fig. 5B). However, unanesthetized mice at P10 showed longer bursts of 10–25 action potentials occurring at the peaks of complex depolarizations lasting 15–25 s (Fig. 5B). At P20, frequent brief (200–400 ms) subthreshold depolarizations occurred at a frequency of 2–3 Hz. The membrane potential trajectory during these depolarizations resulted in a skewed unimodal membrane potential distribution (data not shown). Very few of these depolarizations ($9.0 \pm 7.0\%$) resulted in the firing of action potentials.

It is conceivable that the rapid developmental decorrelation of network activity could result from changes in the intrinsic membrane properties of individual neurons or from changes in excitatory and inhibitory synaptic transmission. Although previous

studies in acute brain slices suggest that these parameters change throughout development (McCormick and Prince, 1987; Maravall et al., 2004a), this has not been studied *in vivo* during the narrow time window in development when we observed the desynchronization of cortical network activity. Using *in vivo* patch-clamp recordings, we found that the input resistance of L2/3 neurons decreased sharply from $355.4 \pm 109.9 \text{ M}\Omega$ at P8–P10 ($n = 7$) to $138.5 \pm 8.8 \text{ M}\Omega$ at P14–P16 ($n = 8$; Mann–Whitney test, $p = 0.0003$) (supplemental Fig. 5A, available at www.jneurosci.org as supplemental material). We also used *in vivo* recordings at a range of membrane potentials to determine the reversal potential of synaptic currents underlying network events (Haider et al., 2006; Waters and Helmchen, 2006). The reversal potential for the peak amplitude and net charge transfer of early network events recorded at P9–P11 was near the excitatory reversal potential (peak amplitude, $-9.2 \pm 2.1 \text{ mV}$; net charge, $-2.3 \pm 1.9 \text{ mV}$; $n = 3$), whereas the reversal potential of network events at P13–P17 was hyperpolarized by $\sim 10 \text{ mV}$ (peak amplitude, $-19.3 \pm 2.3 \text{ mV}$; net charge, $-12.3 \pm 2.8 \text{ mV}$; $n = 3$; $p < 0.05$) (supplemental Fig. 5B, available at www.jneurosci.org as supplemental material). Therefore, both a rapid decrease in the intrinsic excitability of L2/3 neurons and a greater contribution of inhibitory input could contribute to the decreased tendency for action potential firing with each network event after the second postnatal week.

Developmental decorrelation of network activity is not dependent on sensory experience

In barrel cortex, whisker inputs from the periphery are thought to regulate the maturation of neuronal structure (Lendvai et al., 2000) and the receptive fields of L2/3 neurons (Fox, 1992). Similarly, increasing sensory drive as the animal matures could also desynchronize neuronal activity, because uncorrelated peripheral inputs could serve to weaken or disorganize spontaneously correlated activity patterns (Rucci and Casile, 2005). Plucking of whiskers from early neonatal stages weakens the angular tuning of barrel cortical neurons (Simons and Land, 1987) without disrupting the cytoarchitectural and histochemical development of the barrel field (Simons and Land, 1987; Akhtar and Land, 1991; Fox, 1992). Therefore, we expected that this robust method of sensory deprivation would lead to a developmental delay in the desynchronization of network activity. We suppressed peripheral sensory input by plucking the contralateral whiskers starting at P2 and then imaged mice from P9 to P22. Retrospective histological reconstructions were used to confirm

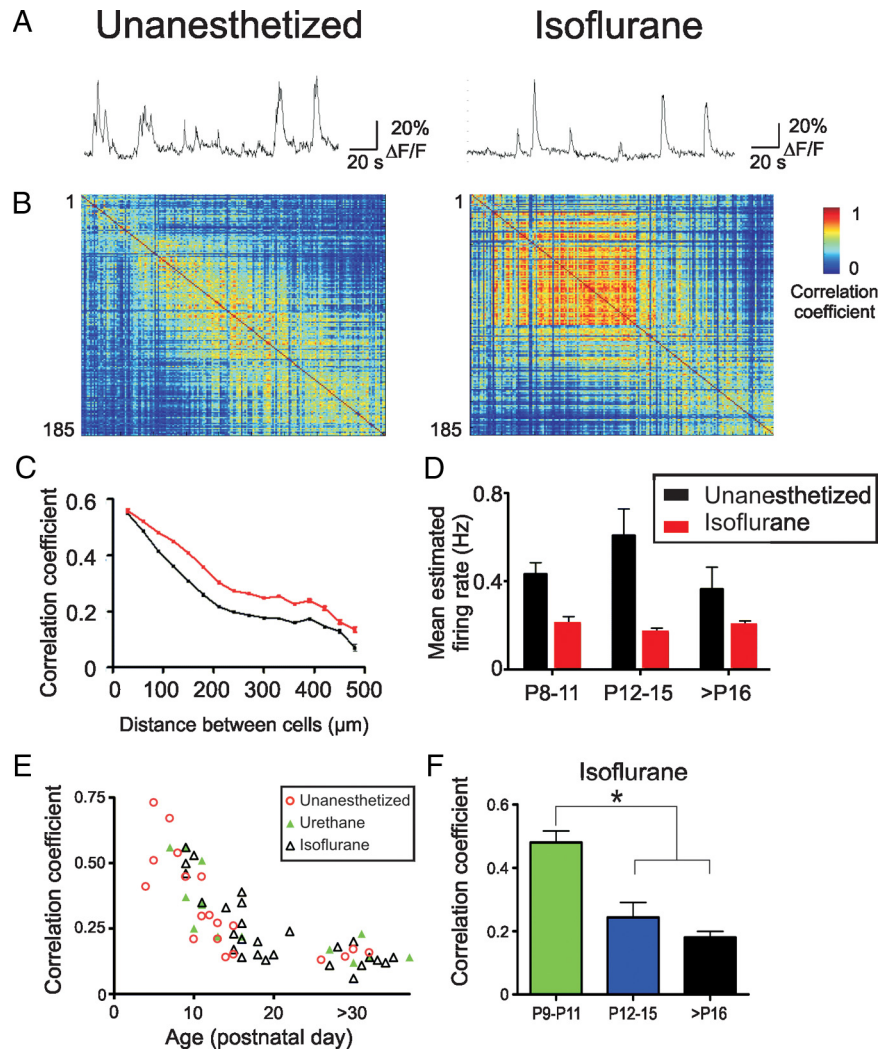


Figure 4. Developmental decorrelation persists under anesthesia. **A**, Average somatic $\Delta F/F$ traces of the same cortical region in the same P9 mouse in the unanesthetized state (left) and under light isoflurane anesthesia (right). **B**, Correlation matrices of deconvolved somatic calcium traces of an ensemble of L2/3 neurons from the same P9 mouse in the unanesthetized state (left) and under light isoflurane anesthesia (right). **C**, Mean correlation coefficient versus distance between cell pairs obtained from the same animal depicted in **A** and **B** in the unanesthetized state (black) and under light isoflurane anesthesia (red). **D**, Mean firing rates estimated from the deconvolved calcium traces in unanesthetized and isoflurane-anesthetized mice, at P8–P11, P12–P15, and older than P16 stages. Error bars in **D** and **F** reflect the SEM. **E**, Mean correlation coefficients of cell pairs located 10–100 μm from each other at different postnatal ages. Pooled data from experiments in unanesthetized (red circles), urethane-anesthetized (green triangles), or isoflurane-anesthetized (black triangles) mice, with each point representing data obtained from a different animal. **F**, Mean correlation coefficients of neuronal pairs separated by 10–100 μm at P9–P11 ($n = 5$), P12–P15 ($n = 9$), and older than P16 ($n = 22$), in isoflurane-anesthetized mice. The asterisk demonstrates statistical significance using a one-way ANOVA, followed by a Tukey's *post hoc* test. Correlation coefficients for all cell pairs within an animal were averaged, and the mean of means was calculated for each developmental stage.

that we imaged barrel cortex (Fig. 6A). For pairs of neurons located within 100 μm , there was no significant difference in the mean correlation coefficient of pairs of cells at P9–P11, P14–P16, or P18–P22 (Student's *t* test, $p = 0.47$, 0.75 , and 0.43 , respectively) (Fig. 6B) between deprived ($n = 3$, 4 , 4 mice, respectively, at each age) and control ($n = 3$, 7 , 3 mice) mice. Similarly, the mean correlation coefficient of cell pairs located 200–500 μm from each other was not altered by sensory deprivation at any age tested (data not shown).

Using our anatomical reconstructions, we could determine where the imaged cells were located with respect to the underlying barrels or septae in L4. In both control and deprived animals, the mean correlation coefficients for cell pairs located above bar-

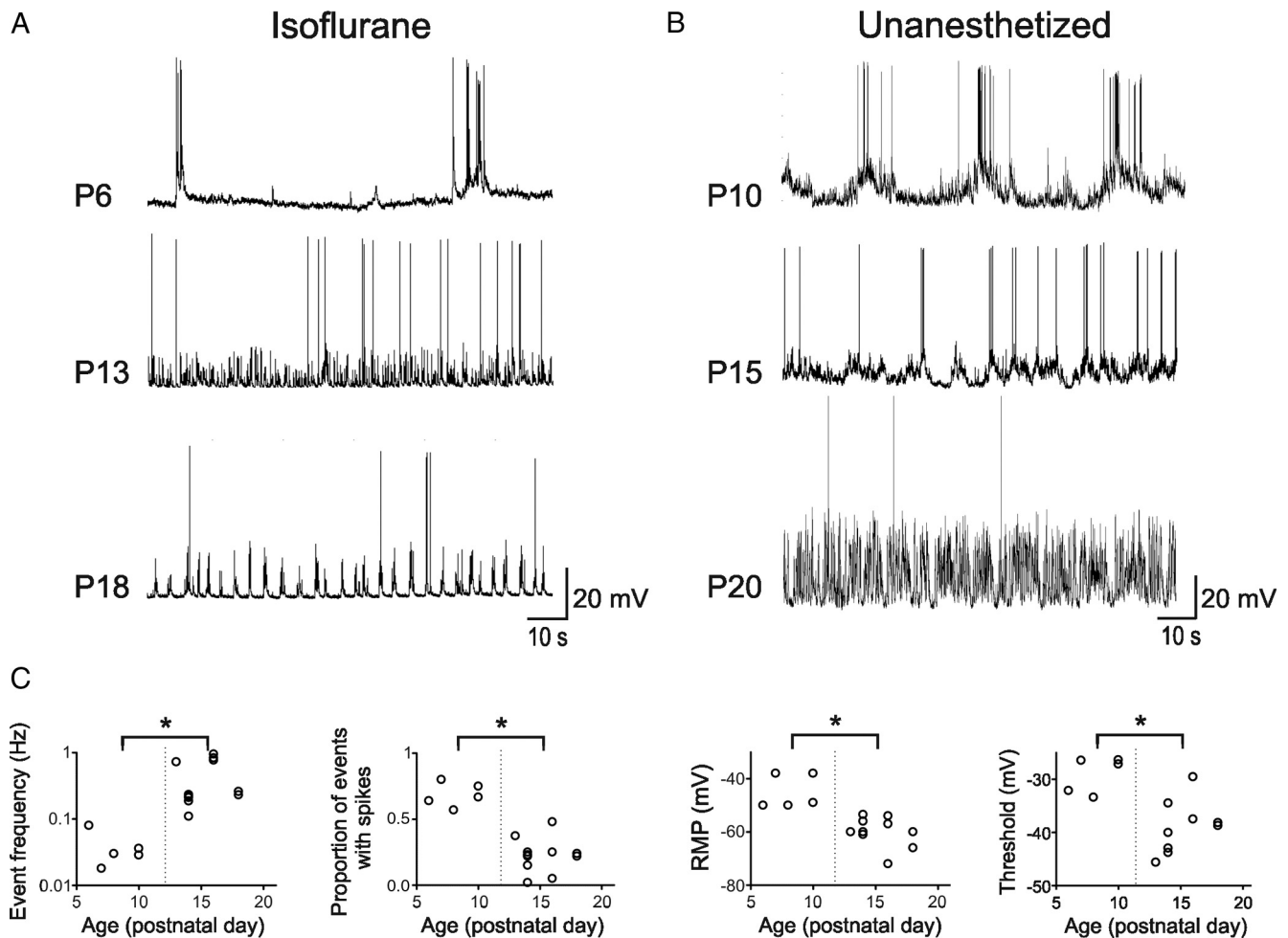


Figure 5. Lower neuronal firing probability per network event after the second postnatal week. *A*, Representative *in vivo* whole-cell recordings from L2/3 neurons at P6, P13, and P18 under light isoflurane anesthesia (0.5–0.8%). *B*, Representative *in vivo* whole-cell recordings from L2/3 neurons in unanesthetized mice at P10, P15, and P20. *C*, Frequency of network events, proportion of network events resulting in the firing of action potentials, resting membrane potential, and action potential threshold across different postnatal ages, in mice under light isoflurane anesthesia. Each point represents data from a single neuron. * $p < 0.05$.

rels versus cell pairs above septae were similar ($p \geq 0.22$) at all distances between cells (Fig. 6C).

Discussion

Synchronized activity in neonatal neocortical networks has been reported *in vitro* (Yuste et al., 1995; Garaschuk et al., 2000; Dupont et al., 2006) and *in vivo* (Chiu and Weliky, 2001; Khazipov et al., 2004; Adelsberger et al., 2005; Hanganu et al., 2006; Minlebaev et al., 2007). The network events we observed at P4–P7 are similar to previously reported spindle bursts (Khazipov et al., 2004) and early network oscillations (Garaschuk et al., 2000; Adelsberger et al., 2005) recorded in neonatal cortical circuits. *In vivo* two-photon calcium imaging in the intact neocortex of unanesthetized mice has enabled us to extend those pioneering studies and examine the contributions of intrinsic cortical synaptic mechanisms and peripheral influences on the evolution of coordinated activity in immature circuits. We find a dramatic change in the spatiotemporal structure of internal dynamics of cortical circuits, which occurs over a few days, at approximately P12: neuronal activity, which is initially highly correlated within small domains of neurons, becomes much less correlated over the range of distances imaged. This change was not attributable to

differences in global neuronal activity, because firing rates remained constant throughout postnatal development.

The significance of synchronous neuronal activity in the first postnatal week is not well understood. One possibility is that it synchronizes neuronal development over functionally related cortical microcircuits. For example, modeling studies suggest that correlated firing during early development can strengthen synapses that receive correlated input leading to the formation of stimulus-selective columns (Song and Abbott, 2001). Therefore, synchronous activity in the first postnatal week could sharpen connectivity maps in cortical neurons receiving inputs from the same whisker. Surprisingly, the small domains of coactive neurons located within ~ 100 – $200 \mu\text{m}$ of each other do not appear to respect barrel boundaries. Additional studies will be needed to examine the underlying substrate for this immature pattern of activity.

The developmental decorrelation of action potential firing is likely to be mechanistically complex. We suggest that developmental changes in the input resistance of cortical neurons and in the contribution of inhibition could play a role in the desynchronization of activity. Other mechanisms may also include a decrease in the number of gap junctions between excitatory neu-

rons throughout postnatal development, but we feel this is unlikely because gap junction blockers fail to eliminate spindle bursts *in vivo* (Hanganu et al., 2006; Minlebaev et al., 2007). Other candidate mechanisms include the expression of glutamate transporters (Voutsinos-Porche et al., 2003), increases in persistent sodium currents (Franceschetti et al., 1998), increases in the number of action potential-independent synaptic potentials (Bazhenov et al., 2002), or changes in presynaptic release probability. It is also possible that a rapid increase in the hyperpolarization-activated cation current (I_h) may play an important role in decreasing neuronal excitability. Indeed, the expression of HCN channels increases steadily after birth to achieve mature levels by the end of the second postnatal week (Zhu, 2000; Vasilyev and Barish, 2002). Increased I_h may diminish the effectiveness of dendritic synaptic potentials from initiating action potentials (Magee, 1999; Fan et al., 2005). Blockade of I_h in slices of ferret prefrontal cortex increases the duration of up states (Vasilyev and Barish, 2002) and causes a nearly fivefold increase in the frequency of action potential firing during up states (Wang et al., 2007) (compare Fig. 5C), suggesting that developmental increases in I_h could limit action potential firing during correlated network events.

Since the landmark work of Hubel and Wiesel in the 1960s (Wiesel and Hubel, 1963; Hubel and Wiesel, 1964), many studies have shown the overwhelming importance of sensory inputs in shaping the structural and functional connectivity of the neocortex (Fox and Wong, 2005). In barrel cortex, whisker plucking results in higher spine turnover (Trachtenberg et al., 2002) and lower dendritic complexity (Maravall et al., 2004b). Functionally, sensory deprivation has profound effects in the tuning of sensory maps in L2/3 neurons, with a loss of angular tuning of barrel cortical neurons (Simons and Land, 1987) and a dramatic reduction in the amplitude of the postsynaptic potential measured in response to deflection of the principal whisker (Lendvai et al., 2000). Surprisingly, the decorrelation of neuronal activity was not dependent on sensory experience. Interestingly, sensory deprivation of barrel cortex does not perturb the development of 7–12 Hz oscillations that precede whisker twitching (Nicollelis et al., 1995).

Our findings have implications for neural coding in neocortex. There is a growing body of evidence that sensory information is encoded sparsely (Olshausen and Field, 2004). In barrel cortex of anesthetized or awake mice, cortical neurons respond on average with a single spike to whisker deflections (Brecht et al., 2003; Kerr et al., 2007; Sato et al., 2007). Indeed, sparse representations are more efficient from both a computational and energetic standpoint (Olshausen and Field, 2004). During wakefulness, decorrelated background activity may increase the efficiency of sparse population codes, improving the coding of natural stimuli. Subtle perturbations in this fundamental step of cortical maturation

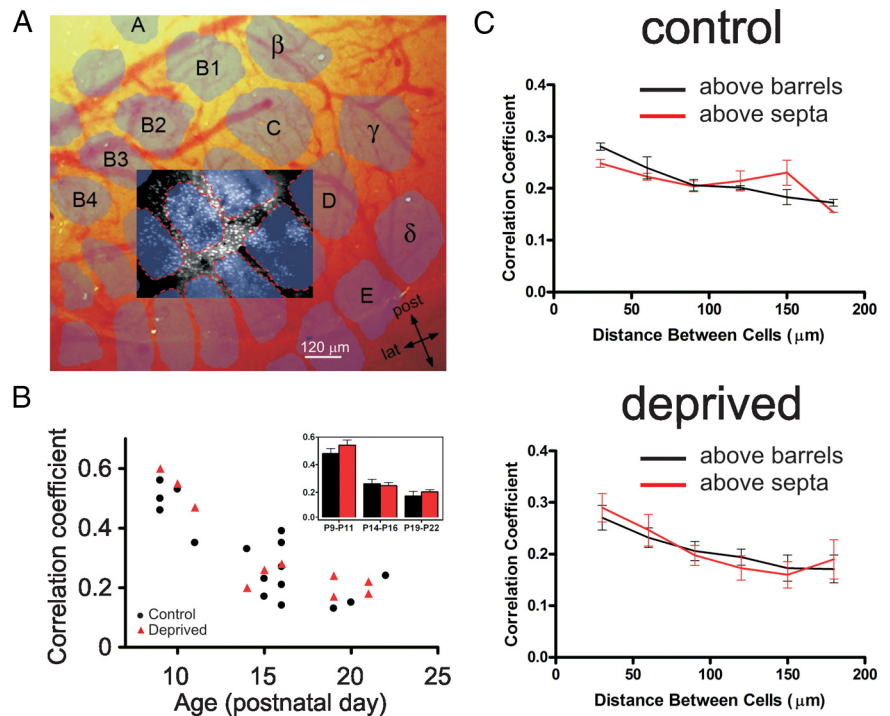


Figure 6. Sensory deprivation does not affect the decorrelation of spontaneous network activity. *A*, *Post hoc* reconstruction of the L4 barrel cytoarchitecture (from cytochrome oxidase staining) in relationship to the OGB-stained neurons in L2/3 previously imaged with *in vivo* two-photon microscopy. The mouse was deprived of whisker input by plucking all contralateral whiskers from P2 until the day of imaging, in this case P15. *B*, Scatter plot and bar graph (inset) of mean correlation coefficients of neuronal pairs located within 10–100 μm of each other for control (black) and deprived (red) mice at P9–P11 ($n = 3$), P14–P16 ($n = 3$), and P19–P22 ($n = 4$). Each point represents a different animal. There are no significant differences. *C*, Mean correlation coefficient versus distance separating pairs of cells located above barrels (black) or above septae (red) at P14–P16, in control (top) or sensory-deprived (bottom) animals. Error bars reflect the SEM.

could result in network dysrhythmias that may underlie a number of disorders, including epilepsy, autism, and schizophrenia.

References

- Adelsberger H, Garaschuk O, Konnerth A (2005) Cortical calcium waves in resting newborn mice. *Nat Neurosci* 8:988–990.
- Akhtar ND, Land PW (1991) Activity-dependent regulation of glutamic acid decarboxylase in the rat barrel cortex: effects of neonatal versus adult sensory deprivation. *J Comp Neurol* 307:200–213.
- Bazhenov M, Timofeev I, Steriade M, Sejnowski TJ (2002) Model of thalamocortical slow-wave sleep oscillations and transitions to activated states. *J Neurosci* 22:8691–8704.
- Brecht M, Roth A, Sakmann B (2003) Dynamic receptive fields of reconstructed pyramidal cells in layers 3 and 2 of rat somatosensory barrel cortex. *J Physiol* 553:243–265.
- Chapman B, Stryker MP (1993) Development of orientation selectivity in ferret visual cortex and effects of deprivation. *J Neurosci* 13:5251–5262.
- Chiu C, Weliky M (2001) Spontaneous activity in developing ferret visual cortex *in vivo*. *J Neurosci* 21:8906–8914.
- Dombeck DA, Khabbaz AN, Collman F, Adelman TL, Tank DW (2007) Imaging large-scale neural activity with cellular resolution in awake, mobile mice. *Neuron* 56:43–57.
- Dreyfus-Brisac C, Larroche JC (1971) Discontinuous electroencephalograms in the premature newborn and at term. *Electro-anatomo-clinical correlations* (in French). *Rev Electroencephalogr Neurophysiol Clin* 1:95–99.
- Dupont E, Hanganu IL, Kilb W, Hirsch S, Luhmann HJ (2006) Rapid developmental switch in the mechanisms driving early cortical columnar networks. *Nature* 439:79–83.
- Fan Y, Fricker D, Brager DH, Chen X, Lu HC, Chitwood RA, Johnston D (2005) Activity-dependent decrease of excitability in rat hippocampal neurons through increases in I_h . *Nat Neurosci* 8:1542–1551.
- Fox K (1992) A critical period for experience-dependent synaptic plasticity in rat barrel cortex. *J Neurosci* 12:1826–1838.

- Fox K, Wong RO (2005) A comparison of experience-dependent plasticity in the visual and somatosensory systems. *Neuron* 48:465–477.
- Franceschetti S, Sancini G, Panzica F, Radici C, Avanzini G (1998) Postnatal differentiation of firing properties and morphological characteristics in layer V pyramidal neurons of the sensorimotor cortex. *Neuroscience* 83:1013–1024.
- Garaschuk O, Linn J, Eilers J, Konnerth A (2000) Large-scale oscillatory calcium waves in the immature cortex. *Nat Neurosci* 3:452–459.
- Garaschuk O, Milos RI, Konnerth A (2006) Targeted bulk-loading of fluorescent indicators for two-photon brain imaging in vivo. *Nat Protoc* 1:380–386.
- Golomb D, Kleinfeld D, Reid RC, Shapley RM, Shraiman BI (1994) On temporal codes and the spatiotemporal response of neurons in the lateral geniculate nucleus. *J Neurophysiol* 72:2990–3003.
- Golshani P, Portera-Cailliau C (2008) In vivo 2-photon calcium imaging in layer 2/3 of mice. *J Vis Exp pii*:681.
- Greenberg DS, Houweling AR, Kerr JN (2008) Population imaging of ongoing neuronal activity in the visual cortex of awake rats. *Nat Neurosci* 11:749–751.
- Haider B, Duque A, Hasenstaub AR, McCormick DA (2006) Neocortical network activity *in vivo* is generated through a dynamic balance of excitation and inhibition. *J Neurosci* 26:4535–4545.
- Hanganu IL, Ben-Ari Y, Khazipov R (2006) Retinal waves trigger spindle bursts in the neonatal rat visual cortex. *J Neurosci* 26:6728–6736.
- Holtmaat A, Wilbrecht L, Knott GW, Welker E, Svoboda K (2006) Experience-dependent and cell-type-specific spine growth in the neocortex. *Nature* 441:979–983.
- Hromádka T, Deweese MR, Zador AM (2008) Sparse representation of sounds in the unanesthetized auditory cortex. *PLoS Biol* 6:e16.
- Hubel DH, Wiesel TN (1964) Effects of monocular deprivation in kittens. *Naunyn-Schmiedeberg Arch Exp Pathol Pharmacol* 248:492–497.
- Iwasato T, Erzurumlu RS, Huerta PT, Chen DF, Sasaoka T, Ulupinar E, Tonegawa S (1997) NMDA receptor-dependent refinement of somatotopic maps. *Neuron* 19:1201–1210.
- Katz LC, Shatz CJ (1996) Synaptic activity and the construction of cortical circuits. *Science* 274:1133–1138.
- Kayser AS, Miller KD (2002) Opponent inhibition: a developmental model of layer 4 of the neocortical circuit. *Neuron* 33:131–142.
- Kerr JN, Greenberg D, Helmchen F (2005) Imaging input and output of neocortical networks in vivo. *Proc Natl Acad Sci U S A* 102:14063–14068.
- Kerr JN, de Kock CP, Greenberg DS, Bruno RM, Sakmann B, Helmchen F (2007) Spatial organization of neuronal population responses in layer 2/3 of rat barrel cortex. *J Neurosci* 27:13316–13328.
- Khazipov R, Luhmann HJ (2006) Early patterns of electrical activity in the developing cerebral cortex of humans and rodents. *Trends Neurosci* 29:414–418.
- Khazipov R, Sirota A, Leinekugel X, Holmes GL, Ben-Ari Y, Buzsáki G (2004) Early motor activity drives spindle bursts in the developing somatosensory cortex. *Nature* 432:758–761.
- Lendvai B, Stern EA, Chen B, Svoboda K (2000) Experience-dependent plasticity of dendritic spines in the developing rat barrel cortex in vivo. *Nature* 404:876–881.
- Louie K, Wilson MA (2001) Temporally structured replay of awake hippocampal ensemble activity during rapid eye movement sleep. *Neuron* 29:145–156.
- Magee JC (1999) Dendritic Ih normalizes temporal summation in hippocampal CA1 neurons. *Nat Neurosci* 2:508–514.
- Maravall M, Stern EA, Svoboda K (2004a) Development of intrinsic properties and excitability of layer 2/3 pyramidal neurons during a critical period for sensory maps in rat barrel cortex. *J Neurophysiol* 92:144–156.
- Maravall M, Koh IY, Lindquist WB, Svoboda K (2004b) Experience-dependent changes in basal dendritic branching of layer 2/3 pyramidal neurons during a critical period for developmental plasticity in rat barrel cortex. *Cereb Cortex* 14:655–664.
- McCormick DA, Prince DA (1987) Post-natal development of electrophysiological properties of rat cerebral cortical pyramidal neurones. *J Physiol* 393:743–762.
- Miller KD (1994) A model for the development of simple cell receptive fields and the ordered arrangement of orientation columns through activity-dependent competition between ON- and OFF-center inputs. *J Neurosci* 14:409–441.
- Miller KD, Erwin E, Kayser A (1999) Is the development of orientation selectivity instructed by activity? *J Neurobiol* 41:44–57.
- Minlebaev M, Ben-Ari Y, Khazipov R (2007) Network mechanisms of spindle-burst oscillations in the neonatal rat barrel cortex in vivo. *J Neurophysiol* 97:692–700.
- Nicolelis MA, Baccala LA, Lin RC, Chapin JK (1995) Sensorimotor encoding by synchronous neural ensemble activity at multiple levels of the somatosensory system. *Science* 268:1353–1358.
- Olshausen BA, Field DJ (2004) Sparse coding of sensory inputs. *Curr Opin Neurobiol* 14:481–487.
- Pologruto TA, Sabatini BL, Svoboda K (2003) ScanImage: flexible software for operating laser scanning microscopes. *Biomed Eng Online* 2:13.
- Poulet JF, Petersen CC (2008) Internal brain state regulates membrane potential synchrony in barrel cortex of behaving mice. *Nature* 454:881–885.
- Rucci M, Casile A (2005) Fixational instability and natural image statistics: implications for early visual representations. *Network* 16:121–138.
- Sato TR, Gray NW, Mainen ZF, Svoboda K (2007) The functional microarchitecture of the mouse barrel cortex. *PLoS Biol* 5:e189.
- Shadlen MN, Newsome WT (1994) Noise, neural codes and cortical organization. *Curr Opin Neurobiol* 4:569–579.
- Shatz CJ, Stryker MP (1988) Prenatal tetrodotoxin infusion blocks segregation of retinogeniculate afferents. *Science* 242:87–89.
- Simons DJ, Land PW (1987) Early experience of tactile stimulation influences organization of somatic sensory cortex. *Nature* 326:694–697.
- Song S, Abbott LF (2001) Cortical development and remapping through spike timing-dependent plasticity. *Neuron* 32:339–350.
- Stosiek C, Garaschuk O, Holthoff K, Konnerth A (2003) In vivo two-photon calcium imaging of neuronal networks. *Proc Natl Acad Sci U S A* 100:7319–7324.
- Trachtenberg JT, Chen BE, Knott GW, Feng G, Sanes JR, Welker E, Svoboda K (2002) Long-term in vivo imaging of experience-dependent synaptic plasticity in adult cortex. *Nature* 420:788–794.
- Vasilev DV, Barish ME (2002) Postnatal development of the hyperpolarization-activated excitatory current I_h in mouse hippocampal pyramidal neurons. *J Neurosci* 22:8992–9004.
- Voutsinos-Porche B, Bonvento G, Tanaka K, Steiner P, Welker E, Chatton JY, Magistretti PJ, Pellerin L (2003) Glial glutamate transporters mediate a functional metabolic crosstalk between neurons and astrocytes in the mouse developing cortex. *Neuron* 37:275–286.
- Wang M, Ramos BP, Paspalas CD, Shu Y, Simen A, Duque A, Vijayraghavan S, Brennan A, Dudley A, Nou E, Mazer JA, McCormick DA, Arnsten AF (2007) Alpha2A-adrenoceptors strengthen working memory networks by inhibiting cAMP-HCN channel signaling in prefrontal cortex. *Cell* 129:397–410.
- Waters J, Helmchen F (2006) Background synaptic activity is sparse in neocortex. *J Neurosci* 26:8267–8277.
- Wiesel TN, Hubel DH (1963) Effects of visual deprivation on morphology and physiology of cells in the cats lateral geniculate body. *J Neurophysiol* 26:978–993.
- Yaksi E, Friedrich RW (2006) Reconstruction of firing rate changes across neuronal populations by temporally deconvolved Ca^{2+} imaging. *Nat Methods* 3:377–383.
- Yuste R, Nelson DA, Rubin WW, Katz LC (1995) Neuronal domains in developing neocortex: mechanisms of coactivation. *Neuron* 14:7–17.
- Zhu JJ (2000) Maturation of layer 5 neocortical pyramidal neurons: amplifying salient layer 1 and layer 4 inputs by Ca^{2+} action potentials in adult rat tuft dendrites. *J Physiol* 526:571–587.
- Zohary E, Shadlen MN, Newsome WT (1994) Correlated neuronal discharge rate and its implications for psychophysical performance. *Nature* 370:140–143.

SUPPLEMENTARY FILES

Supplementary Discussion:

The role of experience in the desynchronization of cortical network activity:

The neocortex is capable of generating its own patterns of activity, presumably as a result of spontaneous activity in the primary sensory organs. For example, in the developing visual system, before eye opening, waves of correlated spontaneous activity periodically sweep across the retina and are propagated to the thalamus and then onto the neocortex (Meister et al., 1991; Wong et al., 1993; Feller et al., 1996; Feller et al., 1997; Penn et al., 1998; Hanganu et al., 2006). Similarly, in the developing somatosensory system, periodic myoclonic jerks in the limbs trigger localized bursts of activity in the neocortex, referred to as spindle bursts (Khazipov et al., 2004). Importantly, this spontaneous activity in the neocortex persists even when it is deprived of inputs from the periphery (Weliky and Katz, 1999; Chiu and Weliky, 2001; Hanganu et al., 2006). This suggests that the developing cortex plays the dominant role in generating the correlated activity within its recurrently connected circuits. Interestingly, blockade of action potential driven activity prevents the clustering of horizontal collaterals in the developing cat visual cortex but enucleation does not (Ruthazer and Stryker, 1996), implying that internally generated activity in the cortex may be sufficient to mediate some aspects of activity-dependent refinement of circuits. Our data extend these findings by demonstrating that even the state transition from highly synchronous to largely sparse and decorrelated firing of neurons is not dependent on sensory inputs, even though it coincides with eye opening and more vigorous sensory exploration of the environment.

Changes in the Balance of Excitation and Inhibition Underlying Developmental Decorrelation

We find an increase in the contribution of inhibitory input after the second postnatal week that could mediate the decorrelation in network activity around P12. However, the technique we used to look at the balance of excitation and inhibition has limitations: because inhibitory postsynaptic currents will not occur at the same precise time within each UP state, it is difficult to determine a precise reversal potential for the composite conductance. Still, the effect of this variability in timing of postsynaptic currents is probably low because we averaged multiple UP states. Furthermore, others have shown a similar time course for the change in the balance of excitation and inhibition in brain slices (Agmon and O'Dowd, 1992).

Given that the chloride equilibrium potential is near its mature hyperpolarized level by P11 in neocortex (Daw et al., 2007) and that bumetanide, which causes a shift in the reversal potential of GABA_A mediated responses, does not block spindle bursts (Minlebaev et al., 2007), we favor a scenario whereby increased activation and recruitment of GABA_A receptors, rather than a shift in the chloride equilibrium potential, leads to decreased neuronal excitability.

Brain states and correlated neuronal firing:

We considered the possibility that different brain states could influence the extent of correlated activity at different ages, as has recently been shown in the adult brain (Poulet and Petersen, 2008). We carefully monitored the behavioral state of most unanesthetized animals used for calcium imaging experiments by closed video circuit. After P12, mice appeared to be in a state of quiet wakefulness and were most likely not asleep. We infer this, because in most videos, brief periods of movement were associated with grooming movements or voluntary changes in posture (not with startle arousals or myoclonus). Furthermore, patch clamp recordings from animals older than P15 showed the presence of

2-5 Hz oscillations, and not the < 1 Hz slow oscillations associated with slow-wave sleep. For animals younger than P12, it was difficult to judge the exact brain state we were observing. The exact delineation of different brain states in neonatal rodents is controversial (Blumberg et al., 2005). Many investigators believe that before the emergence of slow-wave sleep in neonatal mice, brain states may be undifferentiated, and cannot be further characterized (Frank and Heller, 2003, 2005).

To address this concern (i.e., different brain states at different ages could explain the developmental desynchronization of activity), we subjected mice at different postnatal ages to the same brain state by anesthetizing the animals with two anesthetics, isoflurane or urethane. As reported in Fig. 2, we found that while these anesthetics have small effects on the magnitude of correlation coefficients (Suppl. Fig. 4), the time course of developmental decorrelation was identical to that seen in unanesthetized mice. Given that these two anesthetics have different mechanisms of action, the data indicate that this decorrelation is a very robust phenomenon and is present regardless of the brain state of the animal.

Open questions regarding cell-type specific and laminar differences in correlational structure of neocortical networks:

Our study did not differentiate between excitatory cortical neurons and the various subtypes of inhibitory neurons. It is possible that the distribution of correlation coefficients of inhibitory-inhibitory, and inhibitory-excitatory pairs will be different from excitatory-excitatory pairs. This is likely given that excitatory \rightarrow inhibitory connections are usually stronger than excitatory \rightarrow excitatory connections, and spikes in one or few excitatory neurons can drive inhibitory neurons to fire (Bartho et al., 2004). In addition, we focused on the correlational structure within L2/3. It is possible that inter-and intra-laminar correlations between and within other layers could be different. This is likely true for L5, where studies

show that L5 neurons spike on almost every cycle of the slow cortical oscillation (Luczak et al., 2007).

Further studies are needed to address these important questions.

References:

- Agmon A, O'Dowd DK (1992) NMDA receptor-mediated currents are prominent in the thalamocortical synaptic response before maturation of inhibition. *J Neurophysiol* 68:345-349.
- Bartho P, Hirase H, Monconduit L, Zugaro M, Harris KD, Buzsaki G (2004) Characterization of neocortical principal cells and interneurons by network interactions and extracellular features. *J Neurophysiol* 92:600-608.
- Blumberg MS, Karlsson KA, Seelke AM, Mohs EJ (2005) The ontogeny of mammalian sleep: a response to Frank and Heller (2003). *J Sleep Res* 14:91-98.
- Chiu C, Weliky M (2001) Spontaneous activity in developing ferret visual cortex in vivo. *J Neurosci* 21:8906-8914.
- Daw MI, Ashby MC, Isaac JT (2007) Coordinated developmental recruitment of latent fast spiking interneurons in layer IV barrel cortex. *Nat Neurosci* 10:453-461.
- Feller MB, Wellis DP, Stellwagen D, Werblin FS, Shatz CJ (1996) Requirement for cholinergic synaptic transmission in the propagation of spontaneous retinal waves. *Science* 272:1182-1187.
- Feller MB, Butts DA, Aaron HL, Rokhsar DS, Shatz CJ (1997) Dynamic processes shape spatiotemporal properties of retinal waves. *Neuron* 19:293-306.
- Frank MG, Heller HC (2003) The ontogeny of mammalian sleep: a reappraisal of alternative hypotheses. *J Sleep Res* 12:25-34.
- Frank MG, Heller HC (2005) Unresolved issues in sleep ontogeny: a response to Blumberg et al. *J Sleep Res* 14:98-101.
- Hanganu IL, Ben-Ari Y, Khazipov R (2006) Retinal waves trigger spindle bursts in the neonatal rat visual cortex. *J Neurosci* 26:6728-6736.
- Khazipov R, Sirota A, Leinekugel X, Holmes GL, Ben-Ari Y, Buzsaki G (2004) Early motor activity drives spindle bursts in the developing somatosensory cortex. *Nature* 432:758-761.
- Luczak A, Bartho P, Marguet SL, Buzsaki G, Harris KD (2007) Sequential structure of neocortical spontaneous activity in vivo. *Proc Natl Acad Sci U S A* 104:347-352.
- Meister M, Wong RO, Baylor DA, Shatz CJ (1991) Synchronous bursts of action potentials in ganglion cells of the developing mammalian retina. *Science* 252:939-943.
- Minlebaev M, Ben-Ari Y, Khazipov R (2007) Network mechanisms of spindle-burst oscillations in the neonatal rat barrel cortex in vivo. *J Neurophysiol* 97:692-700.
- Penn AA, Riquelme PA, Feller MB, Shatz CJ (1998) Competition in retinogeniculate patterning driven by spontaneous activity. *Science* 279:2108-2112.
- Poulet JF, Petersen CC (2008) Internal brain state regulates membrane potential synchrony in barrel cortex of behaving mice. *Nature* 454:881-885.
- Ruthazer ES, Stryker MP (1996) The role of activity in the development of long-range horizontal connections in area 17 of the ferret. *J Neurosci* 16:7253-7269.
- Weliky M, Katz LC (1999) Correlational structure of spontaneous neuronal activity in the developing lateral geniculate nucleus in vivo. *Science* 285:599-604.
- Wong RO, Meister M, Shatz CJ (1993) Transient period of correlated bursting activity during development of the mammalian retina. *Neuron* 11:923-938.

Supplemental Data Figure Legends

Supplemental Figure S1:

A-B Somatic $\Delta F/F$ calcium traces and simultaneous cell-attached recordings for 2 individual neurons stained with Fluo-4 and imaged at 15.6 Hz in a P13 mouse anesthetized with isoflurane. The actual firing rate as determined from electrophysiological recordings (black) and the calculated firing rate from deconvolved somatic calcium trace (red) are also shown for each neuron. These conditions are identical to those used to generate data shown in Supplemental Fig. S6.

C-E: Somatic $\Delta F/F$ calcium traces and simultaneous cell-attached recordings for 3 individual neurons stained with OGB and imaged at 3.9 Hz from P15 and P19 mice anesthetized with isoflurane (C and D) and from a P15 mouse anesthetized with urethane (E). These conditions (indicator, objective, acquisition speed, anesthesia) are identical to those used to generate data shown in Figs. 4 and 6. They are also identical to conditions in experiments shown in Figs. 1 and 2, except that those data were generated in unanesthetized mice.

F: Somatic $\Delta F/F$ calcium traces and simultaneous cell-attached recordings for one neuron stained with OGB and imaged at 15.6 Hz and simultaneous cell-attached recording in an unanesthetized P12 mouse. These traces should be compared with panels A and B, obtained with Fluo-4 (see also Supplemental Table 1).

G. Graph of simulated data demonstrating a stable ratio of the mean correlation coefficients of early vs. late developmental stages after exclusion of 10-65 % of single spikes. Arrows represent the percentage

of single spikes missed with Fluo-4 and OGB using 20X and 40X objectives at 3.9 and 15.6 Hz imaging frequency in experiments with simultaneous cell-attached recordings and in vivo calcium imaging. Single spikes were defined as spikes separated in time from other spikes by more than 300 ms.

Supplemental Figure S2:

Somatic $\Delta F/F$ calcium traces from 5 representative L2/3 neurons at four postnatal ages, expanded from Fig. 1C.

Supplemental Figure S3:

A. Each graph demonstrates the first singular value squared (the first eigenvalue) from the singular value decomposition of the extrapolated firing rate matrix (red arrow) and the distribution of the first *null* eigenvalues from 100 circularly shuffled firing rate matrices (blue). Note that the first eigenvalues at P5 and P9 (arrows) are far outliers compared to the tightly distributed *null* values. Data from 4 different representative experiments in unanesthetized mice at a range of developmental stages are shown.

B. Graph demonstrating the ratio of the first eigenvalues to first ten median eigenvalues values obtained from 100 shuffled firing rate matrices at P4-P7, P8-P11, P12-P15, and > P16 stages.

Supplemental Figure S4:

A: Average neuropil $\Delta F/F$ calcium traces in L2/3 at P5, P8, P11, P13, P18, >P30.

B. Left: Four consecutive images of OGB loaded L2/3 neurons at P15 with each separated from the next by 6 μm in the z dimension. Arrowheads demonstrate a layer 2/3 neuron sectioned through the equator (filled arrowhead). Right: contours of cells were automatically detected in the image using custom written routines in ImageJ and MATLAB, at settings designed to detect the maximal number of cells (top), and at settings designed to detect only optimally sectioned cells. The cut off boundaries for the cross-section area of optimally sectioned cells were measured from image stacks where individual slices were collected at 2- μm intervals through L2/3 at P10 and P15.

C: Graph demonstrating the relationship of correlation coefficient vs distance separating cell pairs at P8-11 and P14-P16, solely from optimally sectioned cells.

Supplemental Figure S5:

A. Mean correlation coefficient vs. normalized distance between pairs of cells at P4-P7, P8-P11, P12-P15 and >P16 (unanesthetized mice; same data as Fig. 2B). Normalization was performed to correct for the increase in distance between neighboring cells during development.

B. Mean distance separating neighboring neurons at P4-P7, P8-P11, P12-P15 and >P16 stages.

Supplemental Figure S6:

A. Somatic $\Delta F/F$ calcium traces from 5 representative L2/3 neurons stained with Fluo-4 AM at P9 and P14, and imaged under isoflurane with the 40 X 0.8NA objective at 15.6 Hz.

B. Mean correlation coefficients of all pairs of Fluo4-stained neurons located within 100 μm of each other at P6-P9 and P13-15 stages ($n= 2$ and $n= 3$ mice, respectively; Student's t-test: $p < 0.05$).

Supplementary Figure S7: Post-hoc brain reconstruction and registration of two-photon images with barrel architecture.

A. Cartoon of a coronal section of a mouse brain showing the approximate location of the cranial window and the plane of sectioning for reconstructions. Fixed brains were sectioned on a vibratome. The spacing between slices was 60 μm . The slices corresponding to Layer 3 and deeper were processed for cytochrome oxidase (COX) histochemistry.

B. The first step is to create a montage of photographs of individual brain slices, by aligning them with respect to one another (using the contour of the slice, the blood vessel imprints on the edges, and penetrating vessels in brain parenchyma). The slices are ordered from the most superficial (top) to the deepest (bottom). This is done in Adobe Photoshop and is the step that that introduces the largest error in alignment of the imaging field of view with respect to barrel architecture. We estimate this error is $<30 \mu\text{m}$ in the x-y direction for any 2 slices, but is not

cumulative, because it should cancel out when all the slices are registered. The boxed region is shown in higher magnification in panels C-F.

C. Higher magnification of the top 2 slices and a slice through Layer 4 stained with COX, showing individual barrels. The scale bar is the same for panels C-F.

D. Higher magnification view of the aligned brain slices showing the detail of the imprints of the surface vasculature on the cortical surface. Arrows in D-F point to the same vessel bifurcations.

E: The next step is to draw the cortical vessels.

F. These drawings are then used to align the reconstructed brain to the photograph of the same blood vessels as seen through the cranial window (through the two-photon microscope). The edge of the glass coverslip can be seen as a brighter curved streak.

G. Higher magnification view of the blood vessels through the window. The scale bar is the same for panels G-J.

H. A two-photon image stack through Layer 1 from the red channel (taken soon after injection of the OGB-1 AM and Alexa-594 dye mixture) corresponding to the imaged region has been matched to the photograph of blood vessels. This is quite easy because blood vessels can be seen on the two-photon stack as dark shadows. The 512x x 512 image has a lateral dimension of $\sim 720 \mu\text{m}$.

I. Same as H, except the two-photon image is from the green channel showing the OGB-stained neurons in Layer 2/3.

J. Final reconstructed image of the outline (green) of 4 barrels in Layer 4 with the actual imaging field of view for fast calcium imaging.

Supplemental Figure S8:

A. Top: representative in vivo current clamp recordings demonstrating passive responses of L2/3 neurons to 25 pA hyperpolarizing pulses in P10 and P16 mice under light isoflurane anesthesia. Bottom: input resistance of L2/3 neurons at P8-P10 (n= 7) and P14-P16 (n= 8) (* p = 0.0003, Mann-Whitney test).

B. Top: representative in vivo voltage clamp recordings of synaptic currents underlying network events at a range of membrane potentials at P9 and P17. Bottom: extrapolated reversal potential of network events (peak amplitude of the events and net charge transfer) at P9-P11 and P13-P17 (* p < 0.05, Student's t-test; n= 3 for each group). These experiments were performed under light isoflurane anesthesia.

Supplemental Movies:

Movie S1: In vivo calcium imaging with OGB-1AM in a P5 mouse. 3:00 min movie acquired at 3.9 Hz, played here 10 times faster than real time.

Movie S2: In vivo calcium imaging with OGB-1AM in a P9 mouse. 3:00 min movie acquired at 3.9 Hz, played here 10 times faster than real time.

Movie S3: In vivo calcium imaging with OGB-1AM in a P13 mouse. 2:15 min movie acquired at 3.9 Hz, played here 10 times faster than real time.

Movie S4: In vivo calcium imaging with OGB-1AM in a P26 mouse. 3:00 min movie acquired at 3.9 Hz, played here 10 times faster than real time.

Movie S5: In vivo calcium imaging with OGB-1AM in a P6 mouse. 18:00 min movie acquired at 1.95 Hz, played here 10 times faster than real time.

Supplemental Table 1: Correlation of spikes detected by cell-attached electrophysiological recordings to deconvolved calcium traces using OGB and Fluo4, under different acquisition frequencies and with different microscope objectives.

	Correlation coefficient between e-phys and deconvolved trace	Percent of single spikes detected	Percent of spike doublets detected	Percent of bursts of 3 or more action potentials detected
OGB 20X 0.95 NA 3.9 Hz n = 5 cells Figs. 1,2,3,4,6	0.69 ± 0.03	38 ± 13%	80 ± 12%	98 ± 2 %
OGB 40X 0.8 NA 15.6 Hz n = 4 cells	0.83 ± 0.30	63 ± 13%	98 ± 1%	100 ± 0 %
Fluo-4 20X 0.95 NA 15.6 Hz n = 3 cells Fig. S1	0.85 ± 0.05	76 ± 20 %	97 ± 3%	100 ± 0 %
Fluo-4 40X 0.8 NA 15.6 Hz n = 2 cells	0.90 ± 0.02	87 ± 14%	100 ± 0 %	100 ± 0 %

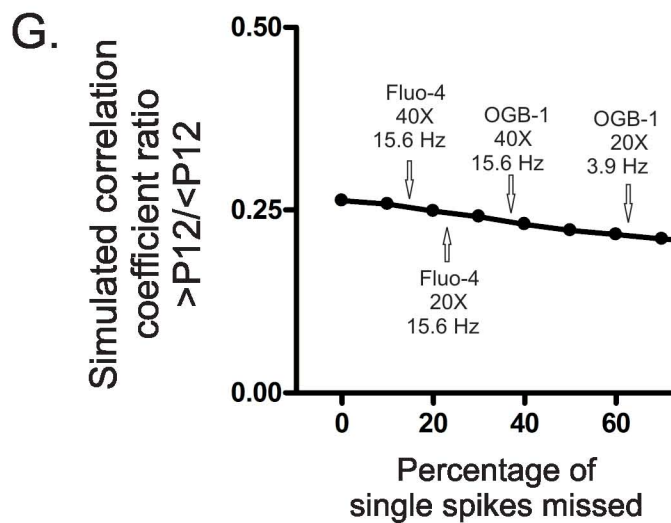
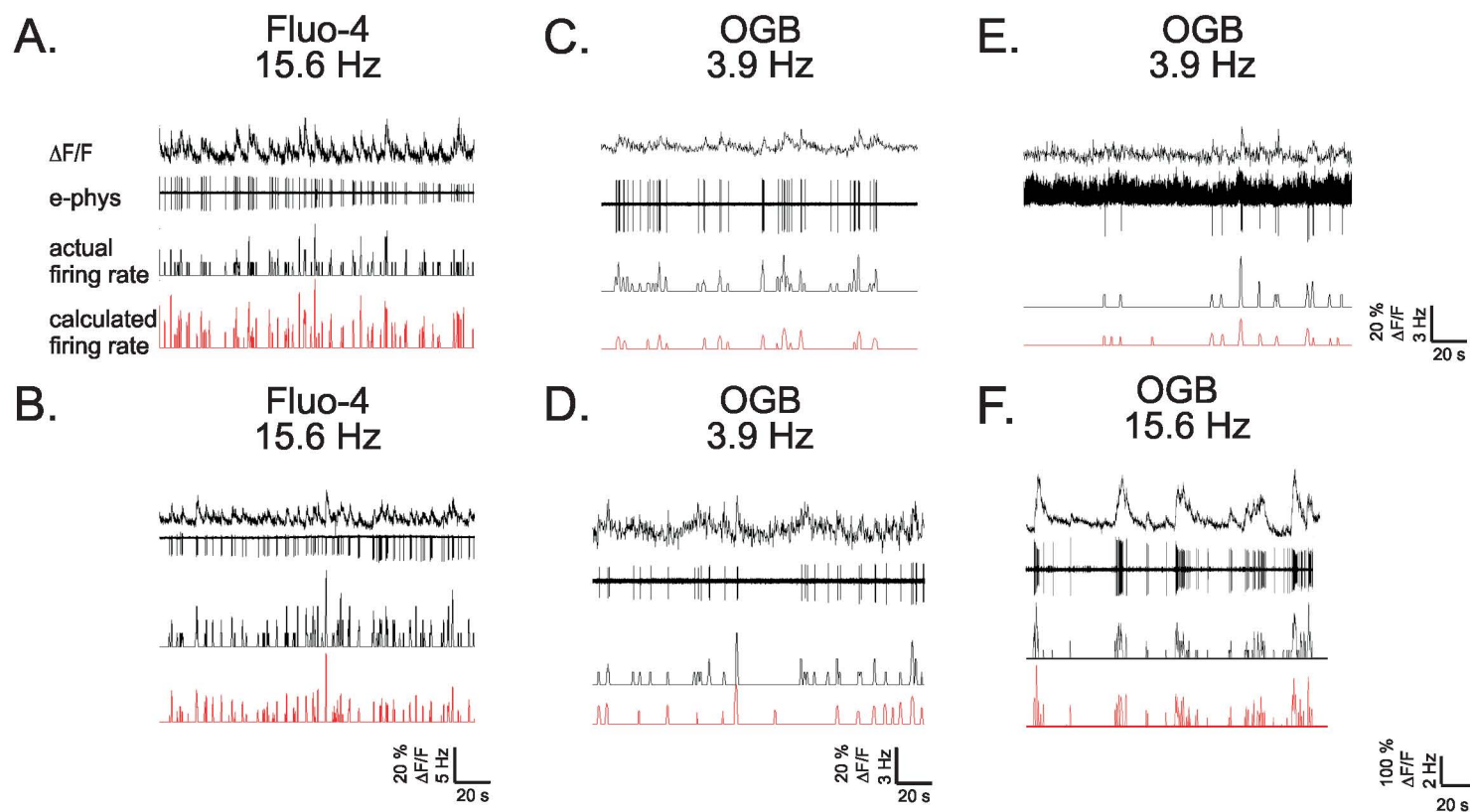
Supplementary Table 2: Developmental changes in network activity as measured by two-photon calcium imaging in unanesthetized mice.

Age	Event Duration (s)	Inter-Event Interval (s)	Mean Correlation Coefficient (All Distances)	Mean Correlation Coefficient (10-100 μm)	Mean Correlation Coefficient (200-500 μm)	Proportion of Cell Pairs Significantly Correlated (10-100 μm)	Proportion of Cell Pairs Significantly Correlated (200-500 μm)
P4-P7 N= 4 mice n=139 events N= 65,106 cell pairs	1.96 \pm 0.10	10.28 \pm 1.60	0.36 \pm 0.05	0.58 \pm 0.09	0.12 \pm 0.07	0.95 \pm 0.02	0.27 \pm 0.17
P8-P11 N= 5 mice n= 121 events N=38,714 cell pairs	2.82 \pm 0.49	23.42 \pm 0.42	0.32 \pm 0.05	0.39 \pm 0.06	0.21 \pm 0.02	0.81 \pm 0.08	0.49 \pm 0.05
P12-P15 N= 6 mice n=172 events N=44,458 cell pairs	1.97 \pm 0.38	13.44 \pm 2.60	0.20 \pm 0.02	0.22 \pm 0.03	0.15 \pm 0.01	0.54 \pm 0.08	0.31 \pm 0.06
>P16 N= 4 mice n=65 events N=9,798 cell pairs	1.28 \pm 0.15	14.34 \pm 6.85	0.15 \pm 0.01	0.15 \pm 0.01	0.14 \pm 0.01	0.31 \pm 0.03	0.24 \pm 0.01

Supplemental Table 3: Average firing rate of cells recorded in whole-cell or cell-attached mode in unanesthetized mice.

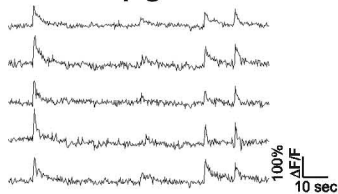
Cell ID	Age	Recording Configuration	Firing Rate (Hz)
032108	P10	Whole-Cell	0.63
021208	P12	Whole-Cell	0.41
021308c1	P15	Whole-Cell	0.20
031108c1	P20	Whole-Cell	0.03
031108c2	P20	Whole-Cell	0.34
021208	P12	Cell-Attached	1.50
013008	P12	Cell-Attached	0.97
020408	P13	Cell-Attached	1.20
021308c2	P15	Cell-Attached	0.15
021308c1	P15	Cell-Attached	0.66
020608	P15	Cell-Attached	0.97
020808	P17	Cell-Attached	0.33

SUPPLEMENTAL FIGURE S1

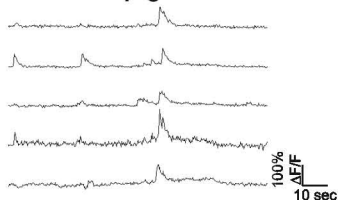


SUPPLEMENTAL FIGURE S2

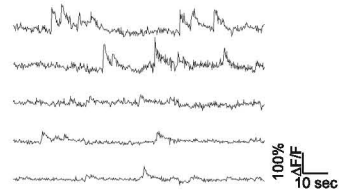
P5



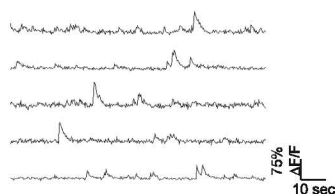
P9



P13

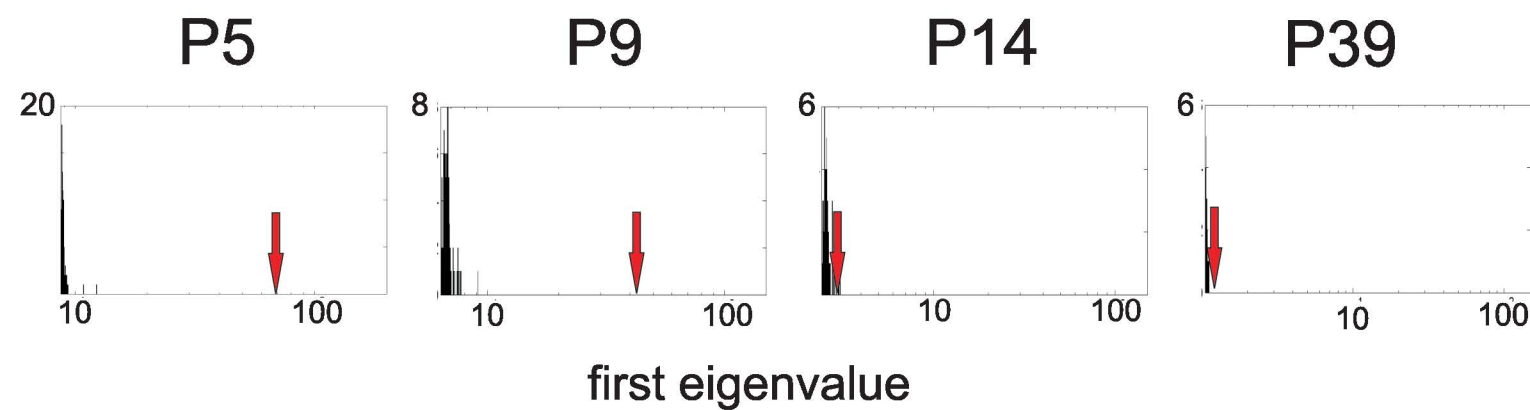


P26

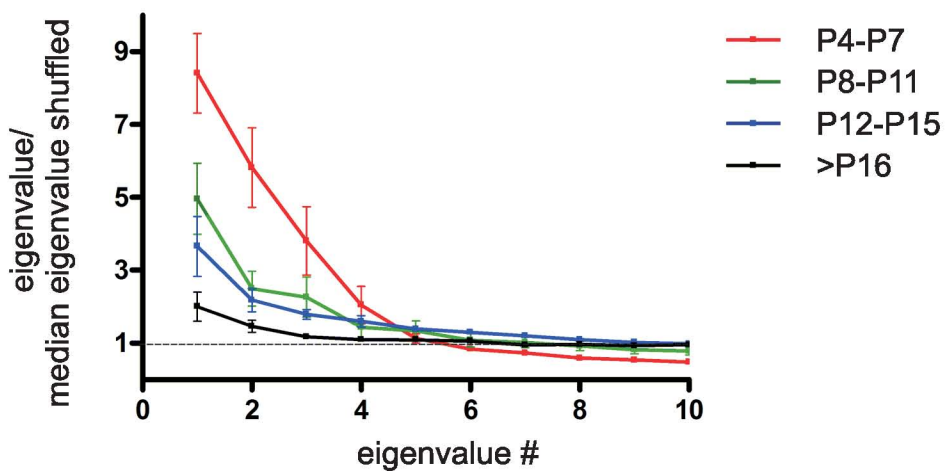


SUPPLEMENTAL FIGURE S3

A.

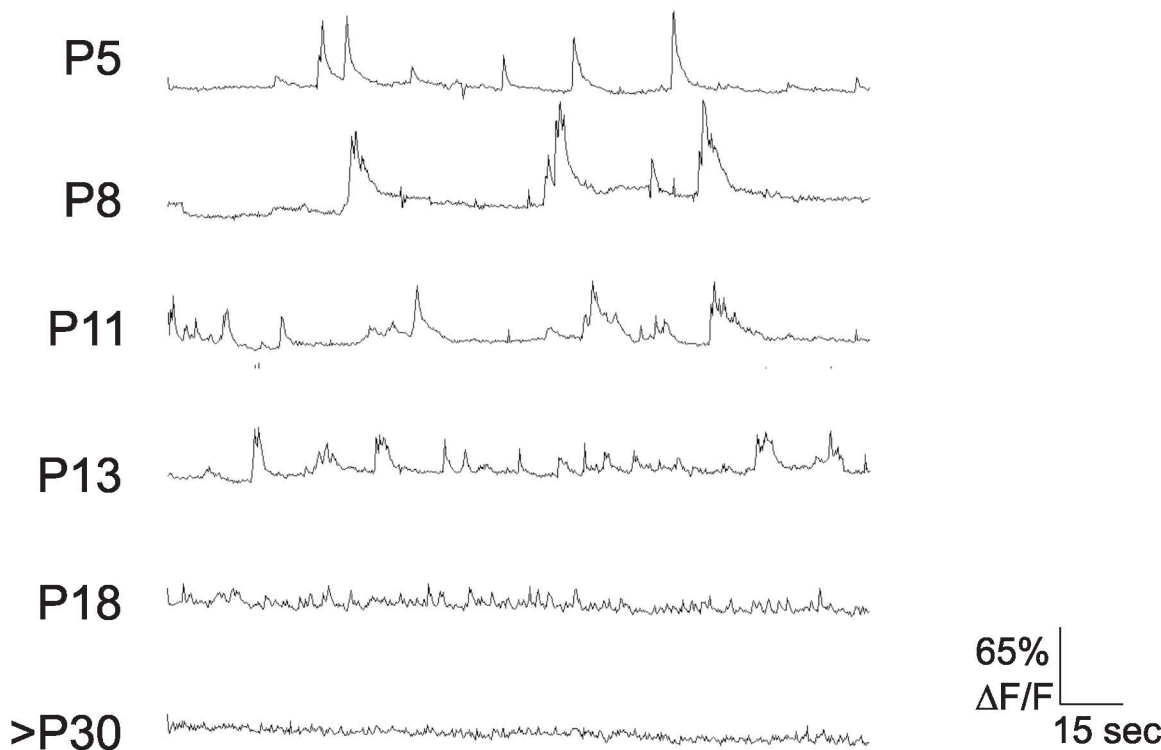


B.

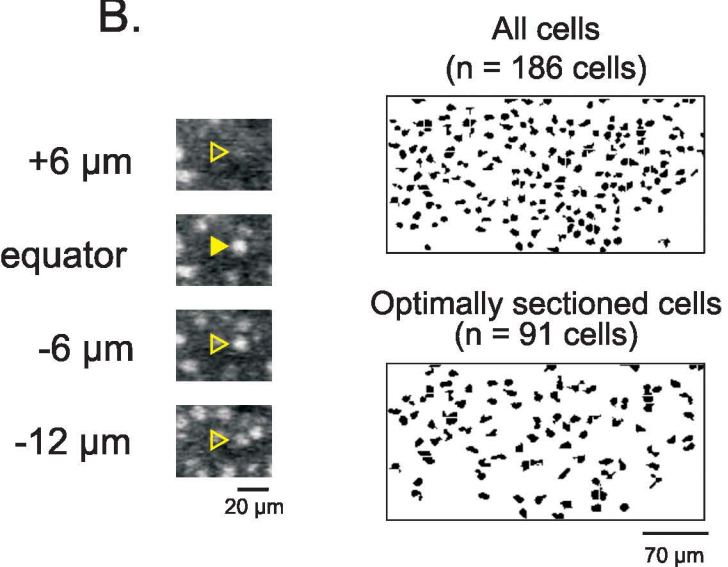


SUPPLEMENTAL FIGURE S4

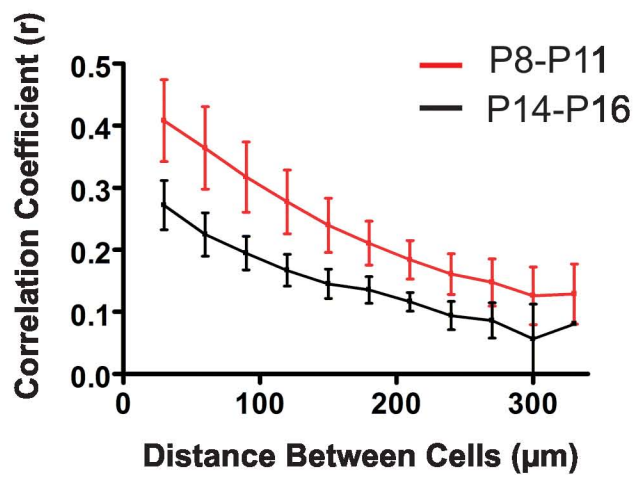
A.



B.

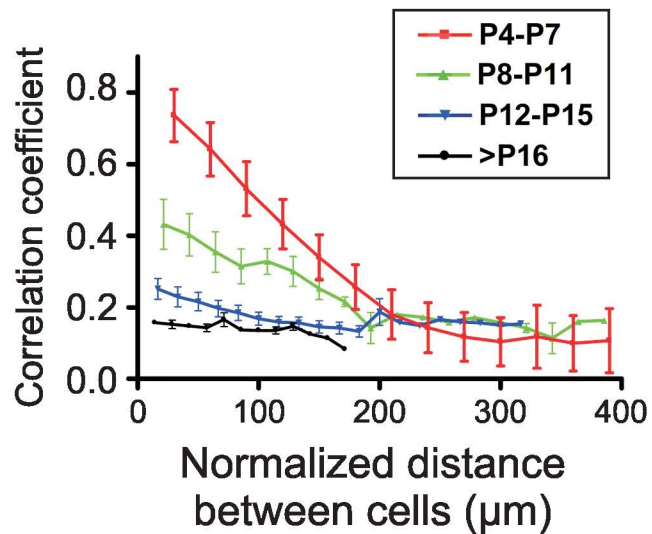


C.

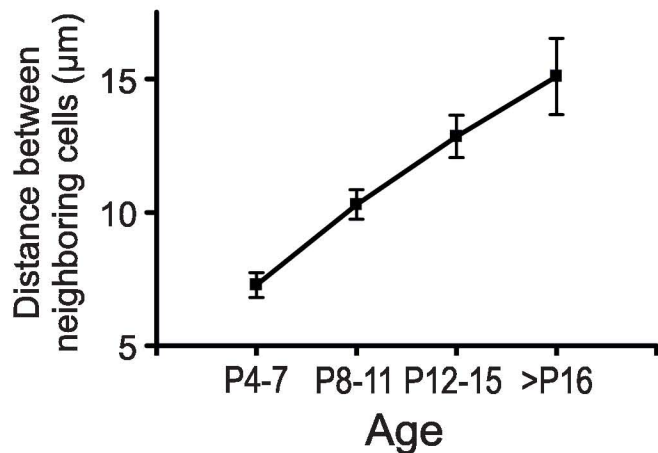


SUPPLEMENTAL FIGURE S5

A



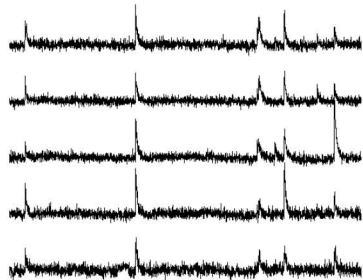
B



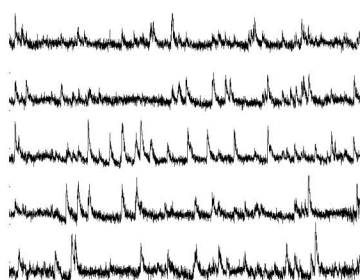
SUPPLEMENTAL FIGURE S6

A

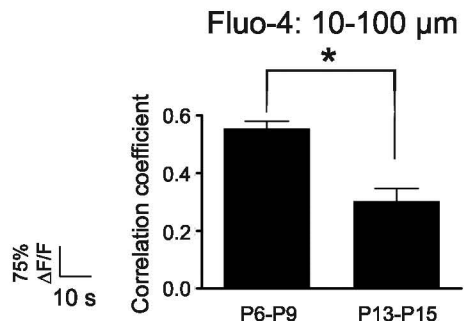
P9

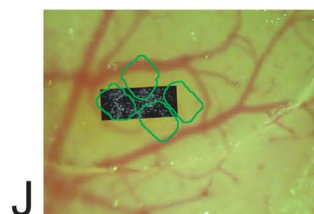
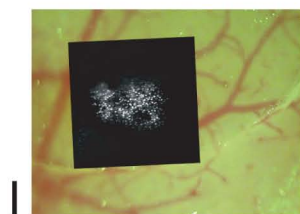
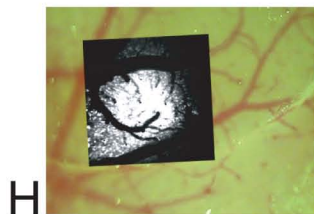
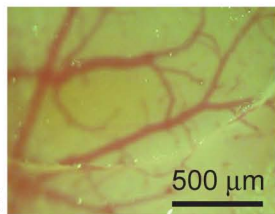
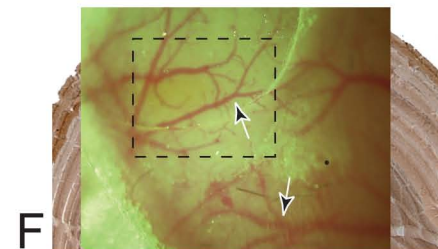
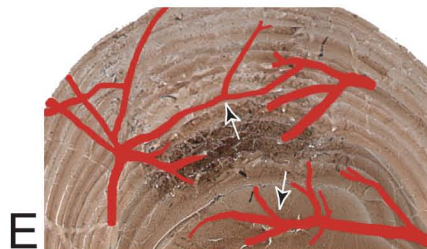
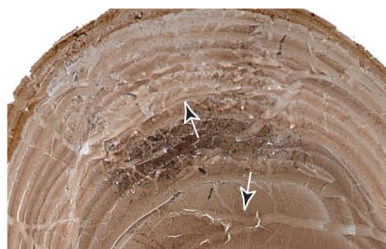
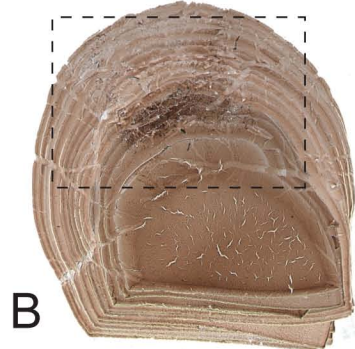
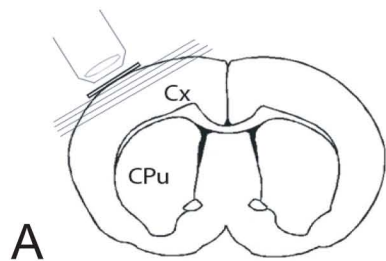


P14



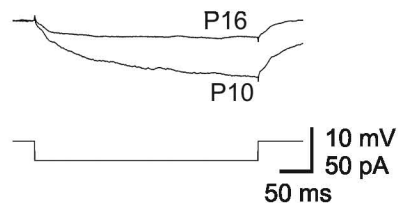
B



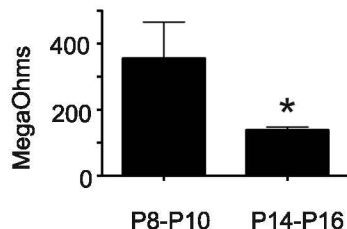


SUPPLEMENTAL FIGURE S8

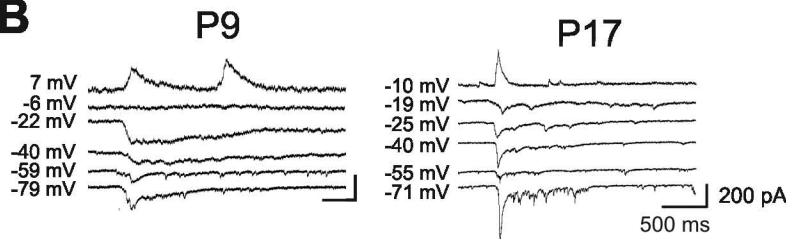
A



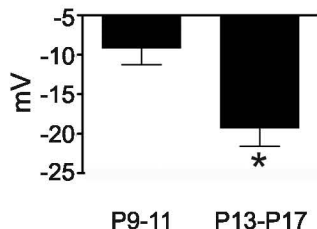
Input resistance



B



Reversal potential
(peak amplitude)



Reversal potential
(charge)

